

# Dual-ratio approach to pulse oximetry and the effect of skin tone

Giles Blaney\*, Jodee Frias, Fatemeh Tavakoli, Angelo Sassaroli, Sergio Fantini

Tufts University, Department of Biomedical Engineering, Medford, MA USA, 02155

## Abstract.

**Significance:** Pulsatile blood Oxygen Saturation ( $\text{SpO}_2$ ) via pulse oximetry is a valuable clinical metric for assessing oxygen delivery. Individual anatomical features, including skin tone, may affect current optical pulse oximetry methods.

**Aim:** Develop an optical pulse oximetry method based on Dual-Ratio (DR) measurements to suppress individual anatomical features on  $\text{SpO}_2$ .

**Approach:** Design a DR-based finger pulse oximeter, hypothesizing that DR would suppress confounds from optical coupling and superficial tissue-absorption. This method is tested using Monte Carlo (MC) simulations and *in vivo* experiments.

**Results:** Different melanosome volume fraction in the epidermis, a surrogate for skin tone, cause changes in the recovered  $\text{SpO}_2$  on the order of 1%. Different heterogeneous pulsatile hemodynamics cause greater changes on the order of 10%.  $\text{SpO}_2$  recovered with DR measurements showed less variability than the traditional Single-Distance (SD) transmission method.

**Conclusions:** For the models and methods considered here,  $\text{SpO}_2$  measurements are more strongly impacted by heterogeneous pulsatile hemodynamics than by melanosome volume fraction. This is consistent with previous reports that, the skin tone bias is smaller than the observed variation in recovered  $\text{SpO}_2$  across individual people. The partial suppression of variability in the  $\text{SpO}_2$  recovered by DR suggests promise of DR for pulse oximetry.

**Keywords:** optical pulse oximetry, blood oxygen saturation, near-infrared spectroscopy, melanin, hemodynamics, dual-ratio.

\*Giles Blaney, Ph.D., [Giles.Blaney@tufts.edu](mailto:Giles.Blaney@tufts.edu)

## 1 Introduction

Pulse oximetry allows for the non-invasive measurement of  $\text{SpO}_2$  (*i.e.*, a surrogate for  $\text{SaO}_2$ ) in various clinical settings.<sup>1-5</sup>  $\text{SpO}_2$  measurements by pulse oximetry have become ubiquitous in modern healthcare, providing valuable real-time assessment of patients' oxygen delivery. The history of pulse oximetry may be considered to start with Glenn Millikan, who invented the first practical oximeter in the 1940s.<sup>1,6</sup> This invention was followed by Takuo Aoyagi's next technological advance in the 1970s when they developed pulse oximetry into something similar to today's technology.<sup>2</sup> However, despite pulse oximetry's widespread adoption and long history, open questions still exist regarding how differences between different people, such as skin tone, would confound the recovered  $\text{SpO}_2$ .<sup>7-14,16</sup> These questions open the door for modern investigations of the technique and the proposal of novel oximetry methods.

Various recent publications have focused on the impact of skin tone on  $\text{SpO}_2$  readings by pulse oximetry. The measurement relies on the ratio of pulsatile optical signals at red and infrared wavelengths. Therefore, the spectral dependence of melanin absorption may result in different confounds at different wavelengths, leading to an error in  $\text{SpO}_2$  when the wrong assumption about skin tone is made. A recent letter examining the measured  $\text{SpO}_2$  versus  $\text{SaO}_2$  on a large population of patients found a positive bias in  $\text{SpO}_2$  for Black versus White patients (*i.e.*, the true  $\text{SaO}_2$  was lower on average for Black patients compared to White who showed the same  $\text{SpO}_2$  reading).<sup>15</sup> Furthermore, other recent studies, reviews, and meta-analyses suggest a similar bias.<sup>8-10,12</sup> In these

cases, the bias is on the order of a few percent on  $\text{SpO}_2$ , but this bias may become more pronounced at lower  $\text{SaO}_2$ .<sup>16</sup>

Further recent studies seek to understand the possible optical origins of these biases and investigate ways to mitigate them by modeling the pulse oximetry measurements using methods such as Monte Carlo (MC) simulations. One such study examined potential confounds affecting the recovered  $\text{SpO}_2$  and found that the modeled  $[M]$  had a slight effect, and its primary impact was on the  $\langle L \rangle$  and the measured  $I$ .<sup>17</sup> A second study utilized similar methods but focused more directly on the effect of  $[M]$  on  $\text{SpO}_2$  calibration, finding a positive bias for darker skin tones around 1% to 2%.<sup>14</sup> Therefore, the biomedical optics field is actively investigating the observed skin tone bias in  $\text{SpO}_2$  measurements, but a definite consensus has yet to be reached. The lack of definite consensus may suggest that there are differences between persons with different skin tones that still need to be fully captured in the current models. Furthermore, new pulse oximetry methods have yet to be proposed that will reduce this bias in the optical measurement itself. These novel methods will be needed so that pulse oximetry can be a valid clinical tool for all patients regardless of skin tone.

In this work, we contribute to the investigation of the effect of skin tone on  $\text{SpO}_2$  measurements and propose a novel pulse oximetry method based on the Dual-Ratio (DR) technique. Our discussion is based on MC simulations and *in vivo* measurements of  $\text{SpO}_2$  on healthy human subjects. The MC model allows us to investigate the effect of the volume fraction of Melanosomes ( $[M]$ ) in the epidermis on pulse oximetry measurements given either homogenous or heterogeneous pulsatile hemodynamics. The novel component is the DR measurement type applied to a human finger. This geometry was inspired by a DR method we developed for measuring absolute optical properties of turbid media in a cuvette.<sup>18</sup> DR<sup>18,19</sup> is a measurement type based on the previously developed Dual-Slope (DS)<sup>20,21</sup> and Self-Calibrating (SC)<sup>22</sup> techniques. These techniques are insensitive to coupling changes and have suppressed  $\mathcal{S}$  near the optodes. These features of DR have the potential to make DR advantageous for  $\text{SpO}_2$  measurements as a result of the small sensitivity to skin-to-optode coupling or dynamics present in superficial tissue (*i.e.*, the epidermis). Therefore, in the following sections, we combine MC models with *in vivo* data to investigate  $[M]$ - or pulsatile-hemodynamic-heterogeneity- based confounds on  $\text{SpO}_2$  and the extent to which those confounds affect either the traditional Single-Distance (SD) measurements in transmittance or the novel DR measurement type applied to finger pulse oximetry.

## 2 Methods

Methods for this work can be divided into two categories: Monte Carlo (MC) simulations ([subsection 2.3](#)) and *in vivo* experimental measurements ([subsection 2.4](#)). Outputs from the MC simulations were used to analyze and interpret the experimental *in vivo* data. We start by describing the measurement geometry ([subsection 2.1](#)) and measurement types ([subsection 2.2](#)) which are common to both.

### 2.1 Measurement geometry

We considered the geometry in [Figure 1](#) for all measurements and simulations in this work. Two source locations and two detector locations were used in a transmission geometry. Sources were named using numbers (1 & 2) while detectors were named using letters (A & B). As shown in [Figure 1\(a\)](#), detector A was placed in-line (*i.e.*, in transmission) with source 1 and, similarly, detector B was in-line with source 2. The spacing between sources 1 and 2 was 20 mm, as shown

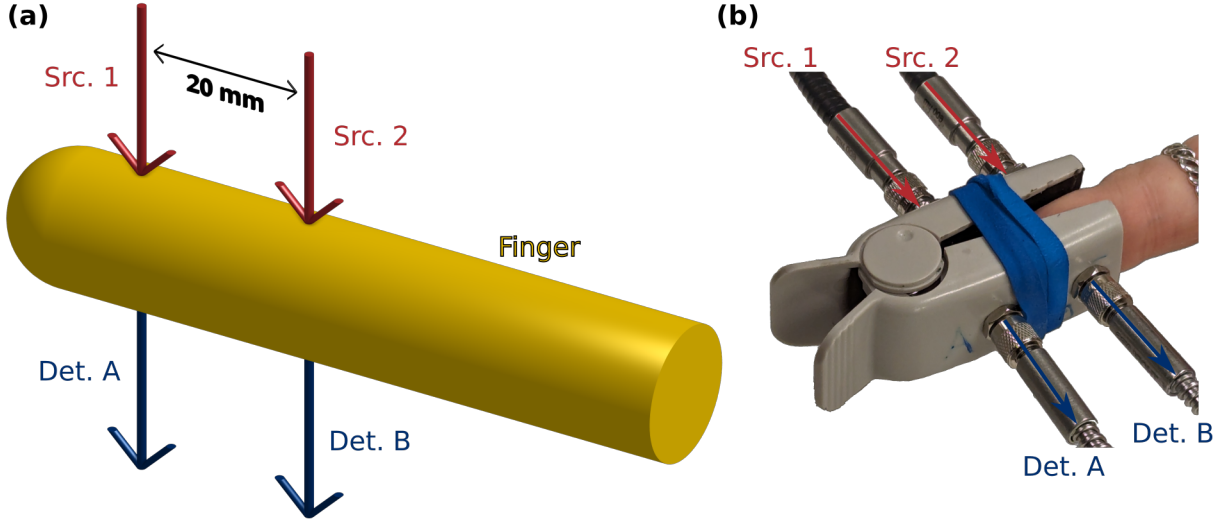


**Fig 1** (a) Schematic of the measurement geometry. Two Sources (Src.; 1 & 2) and two Detectors (Det.; A & B) were utilized in a transmission geometry through the finger to achieve a Dual-Ratio (DR) set. Data were collected from all four possible Single-Distance (SD) source-detector pairs (*i.e.*, 1A, 1B, 2A, 2B). Src. 1/Det. A and Src. 2/Det. B were spaced 20 mm apart. (b) Photo of the probe which utilized four optical fibers (*i.e.*, one for each optode) and a standard pulse-oximeter finger clip. The finger was oriented so the sources were on the nail/knuckle side, and Src. 1 was placed behind the nail such that light did not enter the finger through the nail.

in Figure 1(a). Since corresponding sources and detectors were in-line, detectors A and B were also spaced by the same 20 mm. Figure 1(b) is a photo of the real-life measurement setup which realizes Figure 1(a) using optical fibers and a modified pulse oximetry finger clip.

## 2.2 Measurement types

Two types of measurement are considered in this work, Single-Distance (SD) and Dual-Ratio (DR). SD is the traditional measurement utilized in Near-Infrared Spectroscopy (NIRS) which is based upon the changes (*i.e.*, with respect to baseline) of the natural logarithm of  $I$  measured between one source and one detector. These SD data may be converted to an effective  $\Delta\mu_a$  using the  $\langle L \rangle^a$  according to the following equation:

$$\Delta\mu_{a,SD} = -\frac{\ln [I] - \ln [I_0]}{\langle L \rangle} \quad (1)$$

where  $I_0$  is the baseline Intensity and the subscript SD signifies that the quantity is an effective recovered  $\Delta\mu_a$  from the SD measurement type. For the measurement geometry in this work (Figure 1), there are four SDs (*i.e.*, 1A, 1B, 2A, & 2B), however, for the results in this work, we focus on 1A.

The second measurement type considered here is DR.<sup>18,19</sup> DR is defined as the geometric mean of the ratio between  $I$  measurements at a long and short source-detector distance. Changes in the natural logarithm of this geometric mean can be converted to  $\Delta\mu_a$  using a similar form as

<sup>a</sup>If one wishes to consider the  $\rho$  and the Differential Path-length Factor (DPF) instead, we can write  $\langle L \rangle = \rho\text{DPF}$ .

Equation 1:

$$\Delta\mu_{a,\text{DR}} = -\frac{\ln\left[\sqrt{\frac{I_{1B}I_{2A}}{I_{1A}I_{2B}}}\right] - \ln\left[\sqrt{\frac{I_{1B,0}I_{2A,0}}{I_{1A,0}I_{2B,0}}}\right]}{\Delta\langle L \rangle} \quad (2)$$

where the subscript DR signifies that the quantity is an effective recovered  $\Delta\mu_a$  from the DR measurement type. In this case (*i.e.*, Equation 2), the proportionality constant is the negative inverse of the average difference in total optical path-length ( $\Delta\langle L \rangle$ ) between short and long source-detector distances instead of the negative inverse of  $\langle L \rangle$  as in Equation 1. This,  $\Delta\langle L \rangle$  will be defined later in Equation 6.

In either case, a measurement of  $\Delta\mu_a$  at two or more wavelengths can be converted to a change in Oxy-Hemoglobin concentration ( $\Delta[\text{HbO}_2]$ ) and a change in deoxy-Hemoglobin concentration ( $\Delta[\text{Hb}]$ ) using Beer's law and their known extinction coefficients.<sup>23</sup> For this work, we considered four wavelengths with values of 690 nm, 730 nm, 800 nm and 830 nm.

### 2.3 Monte-Carlo model and simulations

The MC model and simulations in this work used the voxel based Monte-Carlo eXtreme (MCX; rev0313d4 v2020)<sup>24</sup> called from MATrix LABoratory (MATLAB; rev9.14.0.2286388 v2023a). These simulations were run on a desktop computer with Linux Mint 21.1, an AMD Ryzen 9 7950X3D, 128 GB of main memory, and a NVIDIA GeForce RTX 4090 with 24 GB of graphics memory.

Two types of MC simulations were run for two different purposes. The first utilized a coarse voxel size and focused on detecting photons at the detector positions to determine the  $\langle \ell_i \rangle$ , where the different regions (*is*) were associated with different tissue types. This MC to find  $\langle \ell_i \rangle$ s launched  $10^9$  photons and used a voxel size of  $0.25 \text{ mm} \times 0.25 \text{ mm} \times 0.25 \text{ mm}$ . The second MC type utilized a fine voxel size with the goal of generating a high resolution  $\Phi$  spatial distribution. This MC type launched  $10 \times 10^9$  photons and used a voxel size of  $25 \mu\text{m} \times 25 \mu\text{m} \times 25 \mu\text{m}$ . The two MC types utilized a time range of 0 ns to 10 ns with only one time bin so that the results are representative of Continuous-Wave (CW) methods. Additionally, all MC simulations were run three separate times with different random seeds to determine the repeatability of the results.

#### 2.3.1 Finger model

The finger was modeled as an 80 mm long and 15 mm diameter cylinder with a hemisphere at one end to represent the finger-tip (Figure 1(a) and Figure 2). As shown in Figure 2, the coordinate system considered the  $x$ -axis along the length of the cylinder, the  $y$ -axis along the width, and the  $z$ -axis along the height (*i.e.*, nail to pad). The origin was placed with  $x = 0 \text{ mm}$  at the tip of the hemisphere (*i.e.*, the finger-tip),  $y = 0 \text{ mm}$  at the center of the cylinder, and  $z = 0 \text{ mm}$  at the top of the cylinder (*i.e.*, the plane that the sources are incident upon).

Given this coordinate system, source 1 was placed at  $(15\hat{x}) \text{ mm}$ , source 2 at  $(35\hat{x}) \text{ mm}$ , detector A at  $(15\hat{x} + 15\hat{z}) \text{ mm}$ , and detector B at  $(35\hat{x} + 15\hat{z}) \text{ mm}$  (Figure 2). For the first MC type to find  $\langle \ell_i \rangle$ s, the detectors had radii of 1.5 mm so that the detection area was the surface defined by the intersection of a sphere of this radius centered at the detector coordinate and the surface of the cylinder.

Five tissue types were modeled as shells concentric with both the cylinder and hemisphere allowing each tissue type to be characterized by a layer thickness ( $\Delta r$ ; Table 1). These tissue types

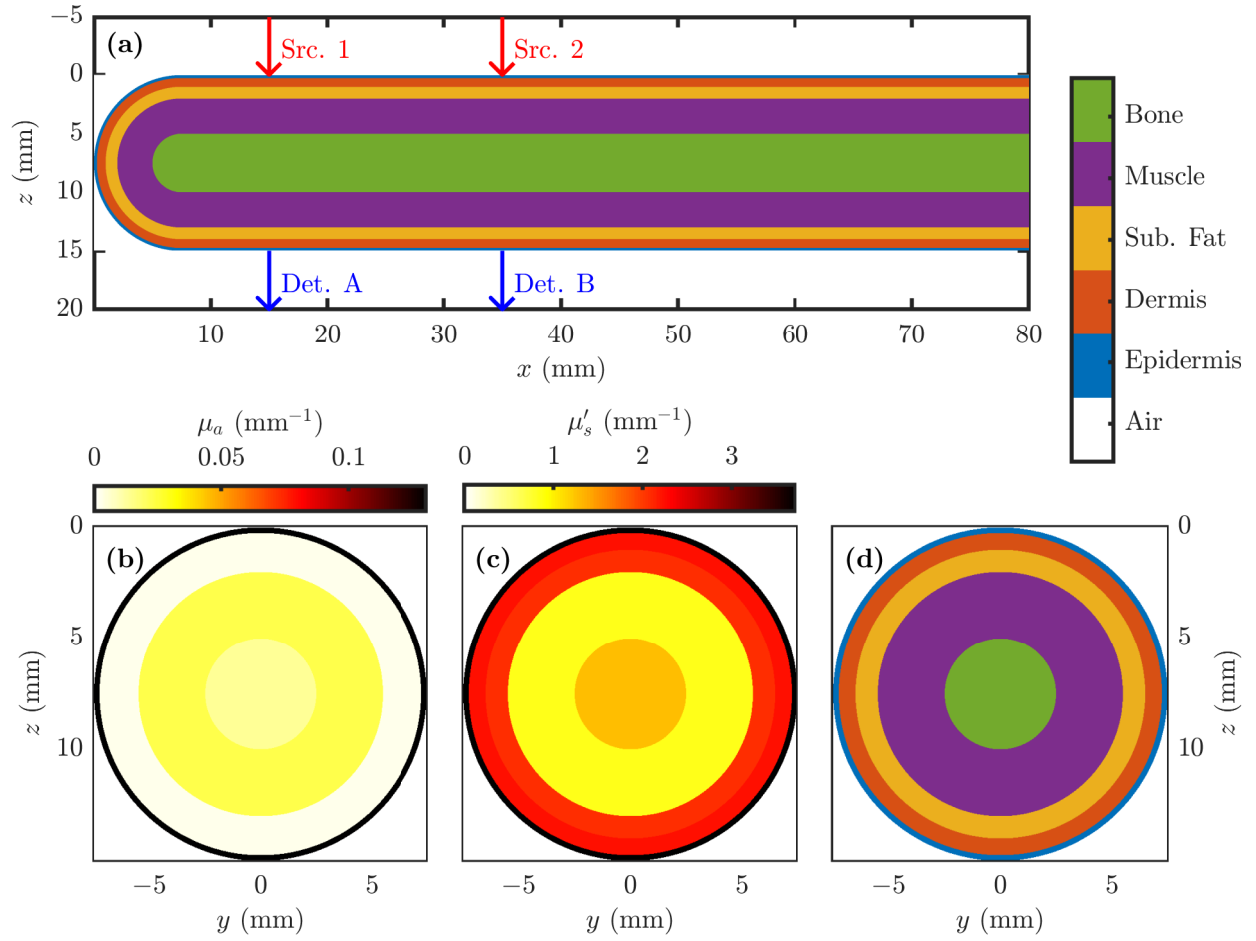


**Fig 2** Monte Carlo (MC) finger model. The model consists of a cylinder 80 mm long and 15 mm in diameter with a 15 mm diameter hemisphere representing the finger tip. Source (Src.) 1 is placed at  $(15\hat{x})$  mm, Src. 2 at  $(35\hat{x})$  mm, Detector (Det.) A at  $(15\hat{x} + 15\hat{z})$  mm, and Det. B at  $(35\hat{x} + 15\hat{z})$  mm. (a)  $xz$  slice at  $y = 0$  mm of the finger model. (b)-(d)  $yz$  slice at  $x = 40$  mm. (b) Map of the absorption coefficient ( $\mu_a$ ) for the lowest volume fraction of Melanosomes ( $[M]$ ) case ( $[M] = 0.013$ ) and the 800 nm wavelength. (c) Map of the reduced scattering coefficient ( $\mu'_s$ ) for the 800 nm wavelength. (d) Slice of the finger model with the same color-scale as (a).

were: epidermis, dermis, subcutaneous-fat (sub. fat), muscle, and bone. Each tissue type was modeled with unique wavelength dependent optical properties, as described in [Table 1](#) and [Table 2](#). The MC simulations were run for each of the four wavelengths (*i.e.*, 690 nm, 730 nm, 800 nm and 830 nm). Furthermore, a range of  $[M]$  was also considered ([Table 2](#)). The first MC type to find  $\langle \ell_i \rangle$ , considered  $[M]$  in the range of 0.013 to 0.430 linearly spaced over 1000 values. The second MC to find  $\Phi$ , considered four values for  $[M]$  of 0.013, 0.152, 0.291 and 0.430. For the most part, chromophore concentrations and optical properties were assigned according to References [25](#) & [26](#). [Table 1](#) and [Table 2](#) specify each specific reference pertinent to each tissue type.

**Table 1** Modeled optical properties and chromophore concentrations in various tissue regions

Tissue	$\lambda$ (nm)	$\mu_a$ ( $\text{mm}^{-1}$ )	$\mu'_s$ ( $\text{mm}^{-1}$ )	$g$	$n$	[HbO <sub>2</sub> ] ( $\mu\text{M}$ )	[Hb] ( $\mu\text{M}$ )	[W] (L/L <sub>tis</sub> )	[L] (L/L <sub>tis</sub> )	$\Delta r^\ddagger$ (mm)
Epidermis <sup>25-30</sup>	690	‡	4.3	0.90	1.48	0.0	0.0	0.20	0.00	0.25
	730	‡	4.1	0.91	1.48					
	800	‡	3.7	0.92	1.48					
	830	‡	3.6	0.92	1.48					
Dermis <sup>25-28,30,31</sup>	690	0.0018	2.6	0.90	1.39	1.8	2.9	0.65	0.00	0.75
	730	0.0022	2.5	0.91	1.39					
	800	0.0023	2.2	0.92	1.39					
	830	0.0029	2.2	0.92	1.39					
Sub. Fat <sup>25-27,30,32,33</sup>	690	0.0023	2.4	0.98	1.49	9.5	3.0	0.11	0.69	1.00
	730	0.0022	2.2	0.98	1.49					
	800	0.0028	2.1	0.98	1.49					
	830	0.0035	2.0	0.98	1.49					
Muscle <sup>25,26,30,34-36</sup>	690	0.025	1.0	0.95	1.37	75	42	0.80	0.00	3.00
	730	0.019	0.9	0.95	1.36					
	800	0.023	0.8	0.95	1.36					
	830	0.026	0.8	0.95	1.36					
Bone <sup>25,26,30,36-41</sup>	690	0.0082	1.4	0.94	1.45	61	8.8	0.32	0.00	2.50
	730	0.0083	1.3	0.94	1.45					
	800	0.014	1.3	0.94	1.45					
	830	0.016	1.3	0.94	1.45					

Symbols: Optical wavelength ( $\lambda$ ), absorption coefficient ( $\mu_a$ ), reduced scattering coefficient ( $\mu'_s$ ), scattering anisotropy ( $g$ ), index of refraction ( $n$ ), Oxy-Hemoglobin concentration ([HbO<sub>2</sub>]), deoxy-Hemoglobin concentration ([Hb]), Water volume fraction ([W]), Lipid volume fraction ([L])

Note †: For bone  $\Delta r$  represents the radius, for other tissues  $\Delta r$  is the radial thickness.

Note ‡: See Table 2.

**Table 2** Modeled absorption coefficient ( $\mu_a$ ) for various volume fraction of Melanosomes ([M])<sup>25,26,29,31,42-45</sup>

$\lambda$ (nm)	$\mu_a$ ( $\text{mm}^{-1}$ )			
	[M] = 0.013	[M] = 0.152	[M] = 0.291	[M] = 0.430
690	0.22	2.6	4.9	7.2
730	0.18	2.1	4.0	5.9
800	0.13	1.5	2.9	4.3
830	0.12	1.3	2.6	3.8

Symbols: Optical wavelength ( $\lambda$ ), absorption coefficient ( $\mu_a$ ), volume fraction of Melanosomes ([M])

### 2.3.2 Calculation of path-lengths and sensitivities

**Monte-Carlo for partial path-lengths** The first MC type was run using a coarse voxel size with the goal to determining the average partial optical path-length in region  $i$  ( $\langle \ell_i \rangle$ ) (*i.e.*, epidermis, dermis, subcutaneous-fat, muscle, and bone) and the average total optical path-length ( $\langle L \rangle$ ) for each source-detector pair.<sup>b</sup> This MC was run white (*i.e.*, with zero  $\mu_a$ ) and the  $\mu_a$  of the various tissue types was applied post-runtime. For each detector (*i.e.*, A or B), the  $\ell$  spent in each type of tissue by each detected photon was saved. For a particular source-detector pair and wavelength, these  $\ell$ s were indexed by tissue region ( $i$ ) and photon number ( $\gamma$ ) so that we have  $\ell_{i,\gamma}$ .

To take into account the  $\mu_a$  of the different tissue regions ( $\mu_{a,i}$ ) post-runtime, each individual  $w_\gamma$  was calculated. This was done by scaling the photon  $w_\gamma$  using Beer-Lambert law as follows:

$$w_\gamma = \prod_i^{N_{\text{regions}}} e^{-\mu_{a,i} \ell_{i,\gamma}} \quad (3)$$

Then these photon weights ( $w_\gamma$ s) were used to calculate the weighted average of  $\ell$ s and yield the average partial optical path-length in region  $i$  ( $\langle \ell_i \rangle$ ) and the average total optical path-length ( $\langle L \rangle$ ) as follows:

$$\langle \ell_i \rangle = \frac{\sum_\gamma^{N_{\text{detected}}} w_\gamma \ell_{i,\gamma}}{\sum_\gamma^{N_{\text{detected}}} w_\gamma} \quad (4)$$

$$\langle L \rangle = \sum_i^{N_{\text{regions}}} \langle \ell_i \rangle \quad (5)$$

where the  $i$  subscript on  $\langle \ell_i \rangle$  represents the tissue region. Unique values of  $\langle \ell_i \rangle$  and  $\langle L \rangle$  were found for each source-detector pair and each wavelength.

$\langle L \rangle$  is the needed proportionality constant in Equation 1 to convert SD  $I$  data to  $\Delta\mu_a$ . For DR we need the  $\overline{\Delta\langle L \rangle}$  in Equation 2 to convert DR  $I$  data to  $\Delta\mu_a$ . To find  $\overline{\Delta\langle L \rangle}$  we consider the  $\langle L \rangle$  for each source-detector pair (*i.e.*, 1A, 1B, 2A, & 2B), and  $\overline{\Delta\langle L \rangle}$  is calculated as follows:

$$\overline{\Delta\langle L \rangle} = \frac{(\langle L \rangle_{1B} - \langle L \rangle_{1A}) + (\langle L \rangle_{2A} - \langle L \rangle_{2B})}{2} \quad (6)$$

Finally, the last output obtained from this first MC type was the  $\mathcal{S}$  for each tissue region. In the SD case,  $\mathcal{S}$  for tissue region  $i$  is calculated as a ratio of  $\langle \ell_i \rangle$  to  $\langle L \rangle$  as follows:<sup>46,47</sup>

$$\mathcal{S}_{\text{SD},i} = \frac{\langle \ell_i \rangle}{\langle L \rangle} \quad (7)$$

While for the DR case,  $\mathcal{S}$  for tissue region  $i$  is given by the ratio of the average difference in  $\langle \ell_i \rangle$ s

---

<sup>b</sup>A separate MC was run for each source and wavelength, such that  $\langle \ell_i \rangle$ s and  $\langle L \rangle$ s were found for each source-detector pair (*i.e.*, 1A, 1B, 2A, & 2B) and each wavelength (*i.e.*, 690 nm, 730 nm, 800 nm and 830 nm). These MCs were repeated three times to determine uncertainties in the results.

to the average difference in  $\langle L \rangle$ s:<sup>46,47</sup>

$$\mathcal{S}_{\text{DR},i} = \frac{(\langle \ell_i \rangle_{1\text{B}} - \langle \ell_i \rangle_{1\text{A}}) + (\langle \ell_i \rangle_{2\text{A}} - \langle \ell_i \rangle_{2\text{B}})}{(\langle L \rangle_{1\text{B}} - \langle L \rangle_{1\text{A}}) + (\langle L \rangle_{2\text{A}} - \langle L \rangle_{2\text{B}})} \quad (8)$$

In both the SD and DR cases,  $\mathcal{S}_i$  is interpreted as the ratio of the recovered effective  $\Delta\mu_a$  from a measurement (*i.e.*, from Equation 1 or Equation 2) and a true local  $\Delta\mu_{a,i}$  in tissue region  $i$ . This concept is expressed by the following equation:<sup>46,47</sup>

$$\mathcal{S}_i = \frac{\Delta\mu_{a,\text{recovered}}}{\Delta\mu_{a,i}} \quad (9)$$

Furthermore, these definitions lead to the following property of  $\mathcal{S}_i$ s:<sup>46,47</sup>

$$\sum_i^{N_{\text{regions}}} \mathcal{S}_i = 1 \quad (10)$$

which means that a homogeneous  $\Delta\mu_a$  (*i.e.*,  $\Delta\mu_{a,i}$ s are equal regardless of  $i$ ) will result in a measured effective recovered  $\Delta\mu_a$  that is equal to the true homogeneous perturbation.

**Monte-Carlo for fluence rate distribution** The second MC type was run with a fine voxel size with the goal of determining the spatial distributions of the  $\Phi$  and then calculating a high-resolution spatial map of  $\mathcal{S}$ .<sup>c</sup> The outputs of this MC type were the fluence rate ( $\Phi$ ) normalized by source power distributions for a pencil beam placed at each source or detector location. The  $\Phi$  distribution from a pencil beam at the detector locations was found by mirroring the  $\Phi$  distributions from the source locations about the plane defined by  $z = 7.5$  mm. This approach of mirroring to find  $\Phi$  from the detectors is possible due to the symmetry in the modeled geometry (Figure 2).

These  $\Phi$  distributions were used to find  $\mathcal{S}$  distributions based on a method similar to the adjoint method.<sup>48</sup> First, to motivate the adjoint method we write the  $\langle \ell_j \rangle$  with  $V$  in terms of a  $\Phi$  and  $R$ s:<sup>47</sup>

$$\langle \ell_j \rangle = \frac{\Phi [\vec{r}_{\text{src}} \rightarrow \vec{r}_j] R [\vec{r}_j \rightarrow \vec{r}_{\text{det}}]}{R [\vec{r}_{\text{src}} \rightarrow \vec{r}_{\text{det}}]} V \quad (11)$$

The arguments of  $\Phi$  or  $R$  in Equation 11 specify the  $\vec{r}$ s of the voxel field point ( $j$ ), the source (src), or the detector (det). The direction of light transport is specified by the arrows in the argument ( $\rightarrow$ ). Next we approximate the  $R$ s with  $\Phi$ s and apply the reciprocity relation  $\Phi [\vec{r}_j \rightarrow \vec{r}_{\text{det}}] = (n_{\text{det}}^2/n_j^2) \Phi [\vec{r}_{\text{det}} \rightarrow \vec{r}_j]$  which accounts for the  $n$  at the detector<sup>d</sup> and voxel.<sup>49</sup> Considering that  $V$ ,  $R [\vec{r}_{\text{src}} \rightarrow \vec{r}_{\text{det}}]$ , and  $n_{\text{det}}$  are constants that do not depend on voxel position we lump them together into the constant  $\beta$  and rewrite an approximation of Equation 11:

$$\langle \ell_j \rangle \approx \beta \frac{\Phi [\vec{r}_{\text{src}} \rightarrow \vec{r}_j] \Phi [\vec{r}_{\text{det}} \rightarrow \vec{r}_j]}{n_j^2} \quad (12)$$

<sup>c</sup>The first MC type only yielded  $\mathcal{S}$  for the five tissue regions, while the second MC type aims to find  $\mathcal{S}$  for each voxel to create a spatial map.

<sup>d</sup>When applying the adjoint method the  $n$  at the detector is the  $n$  of the medium just below the detector since these voxels below the detector are used to determine the detected  $\Phi$ .



To find  $\beta$ , we can apply Equation 5 and use the  $\langle L \rangle$  found from the first MC type:

$$\beta = \frac{\langle L \rangle}{\sum_j^{N_{\text{voxels}}} \frac{\Phi[\vec{r}_{\text{src}} \rightarrow \vec{r}_j] \Phi[\vec{r}_{\text{det}} \rightarrow \vec{r}_j]}{n_j^2}} \quad (13)$$

for each source-detector pair. After obtaining  $\beta$  using the  $\langle L \rangle$  found from the first MC type, we can use Equation 12 to find an approximation of  $\langle \ell_j \rangle$  for each voxel. Finally, Equation 7 and Equation 8 are used to find  $\mathcal{S}_j$  for each voxel and measurement type to create high-resolution spatial maps of  $\mathcal{S}$ .

### 2.3.3 Simulation of pulsatile hemodynamics and recovered pulsatile saturation

Using the Sensitivity to local absorption change ( $\mathcal{S}$ ) for each tissue region, we can model hemodynamic oscillations (*i.e.*, from cardiac pulsation) in each tissue region and then simulate the associated recovered  $\Delta\mu_a$ . To this aim, we used phasor notation to represent hemodynamic oscillations with a given amplitude and phase at a given frequency (*i.e.*, the heart-rate in this case). These hemodynamic phasors for Oxy-Hemoglobin concentration ( $[\text{HbO}_2]$ ) and deoxy-Hemoglobin concentration ( $[\text{Hb}]$ ) were modeled in each tissue. Then these phasors were converted to  $\mu_a$  phasors in each tissue at each of the four wavelengths using Beer's law and known extinction coefficients.<sup>23,47</sup> Next, the recovered  $\mu_a$  phasors were found by a linear combination of the  $\mu_a$  phasors in each tissue region weighed by the  $\mathcal{S}_i$  in tissue region  $i$  (Equation 9).<sup>47</sup> These simulated recovered  $\mu_a$  phasors at four wavelengths are then converted to recovered  $[\text{HbO}_2]$  and  $[\text{Hb}]$  phasors, again using Beer's law.<sup>23,47</sup> Finally, the  $\text{SpO}_2$  is obtained from these  $[\text{HbO}_2]$  and  $[\text{Hb}]$  phasors ( $[\widetilde{\text{HbO}_2}]$  &  $[\widetilde{\text{Hb}}]$ ) as follows:

$$\text{SpO}_2 = \frac{|[\widetilde{\text{HbO}_2}]|}{|[\widetilde{\text{HbO}_2}]| + |[\widetilde{\text{Hb}}]|} \quad (14)$$

We observe that for  $\text{SpO}_2$  in Equation 14 to be representative of the blood oxygen saturation of a volume oscillating vasculature compartment (*i.e.*, as with  $\text{SaO}_2$ ), the phasors  $[\widetilde{\text{HbO}_2}]$  and  $[\widetilde{\text{Hb}}]$  must be in-phase with each-other.<sup>50</sup> If this is not the case, one needs to apply a correction to take into account the phase difference between  $[\widetilde{\text{HbO}_2}]$  and  $[\widetilde{\text{Hb}}]$ .<sup>51</sup>

For the simulations, the recovered  $\text{SpO}_2$  represents what would be recovered given the modeled hemodynamic phasors in each tissue region. This can be done for either measurement type (*i.e.*, SD or DR) and, in the case of SD, for each source-detector pair (*i.e.*, 1A, 1B, 2A, & 2B). Note that Equation 14 not only applies to simulations but also represents how we calculate  $\text{SpO}_2$  in general for this work, including for the *in vivo* data. We further emphasize that this method of recovering  $\text{SpO}_2$  with Equation 14 from  $[\text{HbO}_2]$  and  $[\text{Hb}]$  phasors individually does not account for the phase relationship between  $[\text{HbO}_2]$  and  $[\text{Hb}]$ .

## 2.4 In vivo measurements

### 2.4.1 Recovery of pulsatile saturation

For the *in vivo* measurements, we used the finger clip probe shown in Figure 1(b) and collected the Intensity ( $I$ ) between each source and detector (*i.e.*, 1A, 1B, 2A, & 2B) and for each wavelength

(*i.e.*, 690 nm, 730 nm, 800 nm and 830 nm).<sup>e</sup> The first step in the analysis of these *in vivo* data was to convert these measured  $I$  to  $\Delta\mu_a$  for each wavelength and measurement type (*i.e.*,  $SD^f$  and DR). This conversion was done using Equation 1 and Equation 2, assuming the  $\langle L \rangle$ s or  $\overline{\Delta\langle L \rangle}$ s obtained from the first MC type described in subsection 2.3.2. Built into this assumption are the finger's optical properties and geometry, including the value of  $[M]$  in the epidermis. Therefore, the *in vivo* data may be analyzed with different assumed values for  $[M]$  ( $[M]_{ass}$ ), to investigate the effect of such assumption.

From the temporal traces of  $\Delta\mu_a$  at the four wavelengths, the temporal  $\Delta[HbO_2]$ s and  $\Delta[Hb]$ s were found using Beer's law.<sup>23</sup> Working with  $\Delta[HbO_2]$  from DR data we next find the heart-frequency (*i.e.*, heart-rate), which is then assumed to be the same for all measurement types within one dataset. To find this frequency, the data were first de-trended so that the first and last temporal points took the value of  $0 \mu M$ . Then, a high-pass filter with a cutoff of 50/60 Hz (*i.e.*, 0.83 Hz) was applied to the signal. Next, the filtered temporal data is transformed into the Fourier domain using a Fast Fourier Transform (FFT) with a Nuttall Blackman-Harris window.<sup>52</sup> Considering only frequencies below 2.5 Hz, the peak in the Fourier domain with the highest amplitude was identified. To find the peak centroid, we considered the peak extending from the first minimum below the frequency of maximum amplitude to the first minimum above the said maximum amplitude frequency point. The centroid frequency was calculated as a weighted average frequency, weighted by the amplitude of each frequency point which comprised the peak; this centroid was taken as the heart-frequency.

Knowing the heart-frequency, the temporal signals of  $\Delta[HbO_2]$  and  $\Delta[Hb]$  associated with each data-type are band-pass filtered about it. The band-pass filter utilized a central frequency equal to the heart-frequency and a bandwidth of 10 mHz.<sup>8</sup> At this point the signals are analyzed in two different ways: an FFT to determine amplitudes and a Hilbert transform to determine phases. For the amplitudes, an FFT of the band-passed signals was taken and the amplitude was determined as the integral of this Fourier spectrum from the beginning to the end of the heart-frequency peak defined as before. The integral bounds are larger than the band-pass bandwidth so that the entire peak is included in the interval. We will write the amplitudes found in this way as  $\left| \widetilde{[HbO_2]} \right|$  and  $\left| \widetilde{[Hb]} \right|$ . To determine the phase of  $\Delta[HbO_2]$  and  $\Delta[Hb]$  at the heart-frequency we employed the Hilbert transform on the band-passed signals. The phase reference was considered to be the phase of the change in total-hemoglobin concentration (*i.e.*,  $\Delta[HbO_2] + \Delta[Hb]$ ) measured by DR. We will write the phases found in this way as  $\angle \widetilde{[HbO_2]}$  and  $\angle \widetilde{[Hb]}$ .

Finally, we utilized the amplitudes,  $\left| \widetilde{[HbO_2]} \right|$  and  $\left| \widetilde{[Hb]} \right|$ , to calculate  $SpO_2$  using Equation 14. These recovered  $SpO_2$  values are obtained for each measurement type but also for different assumed values of  $[M]$ . Therefore, in this work, we investigate how assumed values of  $[M]$  affect the recovered  $SpO_2$ . Further, we will utilize the recovered  $\angle \widetilde{[HbO_2]}$  and  $\angle \widetilde{[Hb]}$  to aid in discussing how phase differences between  $[HbO_2]$  and  $[Hb]$  oscillations affect the recovered  $SpO_2$ .

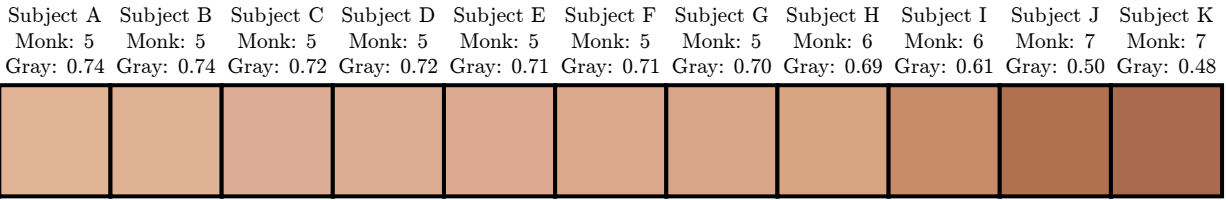


**Fig 3** Color swatches of each subject’s skin tone obtained from a photo of the back of the subject’s hand. For each subject, the Monk scale<sup>53</sup> value and swatch gray-scale value (using Rec.ITU-R BT.601-7) is also reported.

### 2.4.2 Determination of skin tone

To connect the values of  $[M]$  in the MC models with the *in vivo* data, we have quantified the skin tone of the human subjects we measured. For the determination of skin tone we utilized the Monk scale.<sup>53</sup> The Monk scale consists of 10 swatches which represent a wide range of skin tones, with Monk 1 being the lightest and Monk 10 being the darkest.

To determine each subject’s skin tone, a photo of the back of their hand was taken with a Canon EOS Rebel T3i digital camera. For these photos, the stock 18 mm to 55 mm lens was used set at the 55 mm focal-length. The camera took a photo from approximately 1 m distance with a 60 W incandescent light source at almost the same location as the camera. The incandescent light source was the only light source in the room when the photo was taken. The subject’s hand was placed on a white background and the camera focused to the back of the hand. Camera settings were set to full manual and were the same for each subject. The primary camera settings were a ISO of 100, an aperture of  $f/5$ , and an exposure time of 0.3 s. We would like to note that these settings are considered to slightly overexpose the scene, however no part of the images were saturated.

Each photo was saved in the Canon raw image format (CR2) and was 5184 px  $\times$  3456 px in size. A crop of 500 px  $\times$  500 px around the center of the back of the subject’s hand was used for further analysis. This cropped image was averaged to find the average Red-Green-Blue (RGB) color value. These color swatches of the RGB value for each subject are shown in Figure 3. At this point, we note that these RGB color values are comparable between each-other due to the control over camera setup and parameters, but the values would be difficult to compare to color values independently measured by other photographers.

To quantify the subject’s Monk scale value, we compared the subject’s RGB skin-tone value to values derived from photos of Monk scale color swatches. The Monk scale swatches were printed on white paper using a Canon iR ADV C5250 color printer. The printed swatch palette was then photographed with the same settings and at the location as the photos of the subject’s hand. Finally, the determination of Monk scale value for each subject was found by minimizing the difference between the subject’s RGB value and the RGB values for the Monk color swatches. We again note that these values are comparable between subjects in this paper but would be difficult to compare to other photos or Monk scale values determined in different ways. These Monk scale values are reported in Figure 3 and Table 3.

<sup>e</sup>The protocol for these measurements is described in [subsubsection 2.4.3](#).

<sup>f</sup>For this work the SD pair focused upon was 1A.

<sup>g</sup>This small bandwidth filter is needed to apply the Hilbert transform in the next step.

### 2.4.3 Protocol and subjects

**Table 3** Subject information

Subject	Age	Sex at Birth	Monk Skin Tone <sup>53</sup> (See Figure 3)	Race	Ethnicity	Majority Ancestral Region
A	26	Female	5	Multi	Hispanic	North-America
B	31	Female	5	White	Non-Hispanic	Southern-Europe
C	28	Male	5	Asian	Non-Hispanic	Southeast-Asia
D	30	Male	5	White	Non-Hispanic	Northern- & Eastern- Europe
E	23	Female	5	White	Non-Hispanic	Western-Europe
F	25	Male	5	Asian	Non-Hispanic	East-Asia
G	59	Male	5	White	Non-Hispanic	Southern-Europe
H	23	Female	6	Multi	Hispanic	North-America & Southeast-Asia
I	27	Female	6	Asian	Non-Hispanic	Southern-India
J	25	Male	7	Black	Non-Hispanic	Africa
K	29	Male	7	Asian	Non-Hispanic	Southern-India

For all *in vivo* experiments, laser light was delivered to the clip probe (Figure 1(b)) and detected from the clip probe using optical fiber bundles. These fibers delivered light from or to an ISS Imagent V2 Frequency-Domain (FD) NIRS instrument. The FD NIRS instrument used wavelengths of 690 nm, 730 nm, 800 nm and 830 nm, a 140.625 MHz modulation frequency, and a 9.93 Hz sample rate. The amplitude of the FD NIRS data was taken as a close approximation of CW *I* in the context of this work.

Eleven healthy human subjects (*i.e.*, labeled A to K) were recruited and consented according to the Tufts University Institutional Review Board (IRB) protocol for this study. The subjects' age, sex, Monk scale value,<sup>53</sup> race, ethnicity, and majority ancestral region are reported in Table 3. We report racial and ethnic information for each subject to give context on their skin tones beyond our quantification on the Monk scale. Additionally, subjects are ordered A to K in the order of their swatch gray-scale value which corresponds to Monk scale value but with more precision (Figure 3). This order is used to better aid interpretation of the data in terms of skin tone.

For the experimental protocol, each subject was asked to sit in a chair with their left-hand placed on a stool in-front of them, so that their hand was approximately at the height of their chest. All of the subjects in this work reported being right-hand-dominant. Before each experiment we ensured that the subject’s hand was warm, using a space heater when necessary. The subject placed their left-index-finger in the clip probe shown in [Figure 1\(b\)](#); all subjects in this study reported being right handed. The source side of the probe corresponded to the subject’s finger top (*i.e.*, the nail/knuckle side) and the detector side corresponded to the finger bottom (*i.e.*, the pad side). Furthermore, their fingers were placed within the clip probe such that source 1 was just behind the nail (*i.e.*, source light was not transmitted through the nail). Finally, 3 min of NIRS data consisting of the  $I$  between each source and detector was collected for each subject. These data were converted to  $\Delta[\text{HbO}_2]$  and  $\Delta[\text{Hb}]$  then to  $\text{SpO}_2$  for both SD and DR as described in [subsubsection 2.4.1](#).

### 3 Results

#### 3.1 Measurement path-lengths and sensitivities from Monte-Carlo simulations

**Table 4** Monte Carlo (MC) derived average total optical path-lengths ( $\langle L \rangle$ s) and average difference in total optical path-lengths ( $\overline{\Delta \langle L \rangle}$ s); also see [Figure 4](#)

[M]	$\lambda$ (nm)	$\langle L \rangle_{1A}$ (mm)	$\langle L \rangle_{1B}$ (mm)	$\langle L \rangle_{2A}$ (mm)	$\langle L \rangle_{2B}$ (mm)	$\overline{\Delta \langle L \rangle}_{1AB2}$ (mm)
0.013	690	$81.79 \pm 0.02$	$142.2 \pm 0.2$	$141.9 \pm 0.3$	$81.82 \pm 0.02$	$60.2 \pm 0.2$
	830	$73.38 \pm 0.01$	$126.03 \pm 0.06$	$126.3 \pm 0.1$	$73.37 \pm 0.02$	$52.78 \pm 0.07$
0.430	690	$71.92 \pm 0.04$	$128 \pm 1$	$128.0 \pm 0.3$	$71.98 \pm 0.06$	$56.3 \pm 0.6$
	830	$63.70 \pm 0.03$	$112.5 \pm 0.6$	$113.3 \pm 0.3$	$63.76 \pm 0.03$	$49.1 \pm 0.3$

Acronyms: Volume fraction of Melanosomes ([M]), optical wavelength ( $\lambda$ ), average total optical path-length ( $\langle L \rangle$ ), average difference in total optical path-length ( $\overline{\Delta \langle L \rangle}$ )

Note: Values represent the mean of three Monte Carlos (MCs) with different random seeds and the error is half the range of the three MCs.

First, we present the results from the MC simulations. [Figure 4](#) and [Table 4](#) show the  $\langle L \rangle$  from the first MC type. The  $\langle L \rangle$  and the  $\overline{\Delta \langle L \rangle}$  are important since they are the proportionality constants needed to convert optical data (*i.e.*,  $I$ ) to  $\Delta\mu_a$ s ([Equation 1](#) & [Equation 2](#)). Focusing on [Figure 4\(a\)](#), we see that  $\langle L \rangle$  decreases with increasing [M] in the epidermis, with a stronger decrease at lower values of [M]. This is likely due to the photons which take longer paths around the circumference of the finger having a lower probability of surviving when they encounter a more absorbing epidermis. Next, we may examine how [M] affects  $\overline{\Delta \langle L \rangle}$  in [Figure 4\(b\)](#). Here, much like  $\langle L \rangle$ ,  $\overline{\Delta \langle L \rangle}$  also decreases with increasing [M]. However, let’s examine how much  $\langle L \rangle$  or  $\overline{\Delta \langle L \rangle}$  changes from the lowest to highest [M] (*i.e.*, from [M] = 0.013 to [M] = 0.430) at 830 nm using the values in [Table 4](#). In this case  $\langle L \rangle$  changes by  $-13\%$  while  $\overline{\Delta \langle L \rangle}$  changes by  $-7.0\%$ ; we remind that  $\langle L \rangle$  is needed for Single-Distance (SD) measurements while  $\overline{\Delta \langle L \rangle}$  is needed for Dual-Ratio (DR) measurements.

When interpreting these values for  $\langle L \rangle$  and  $\overline{\Delta \langle L \rangle}$  in terms of their relevance toward recovering  $\text{SpO}_2$ , it is important to consider all wavelengths. This is done in [Figure 4\(c\)&\(d\)](#) where the ratio

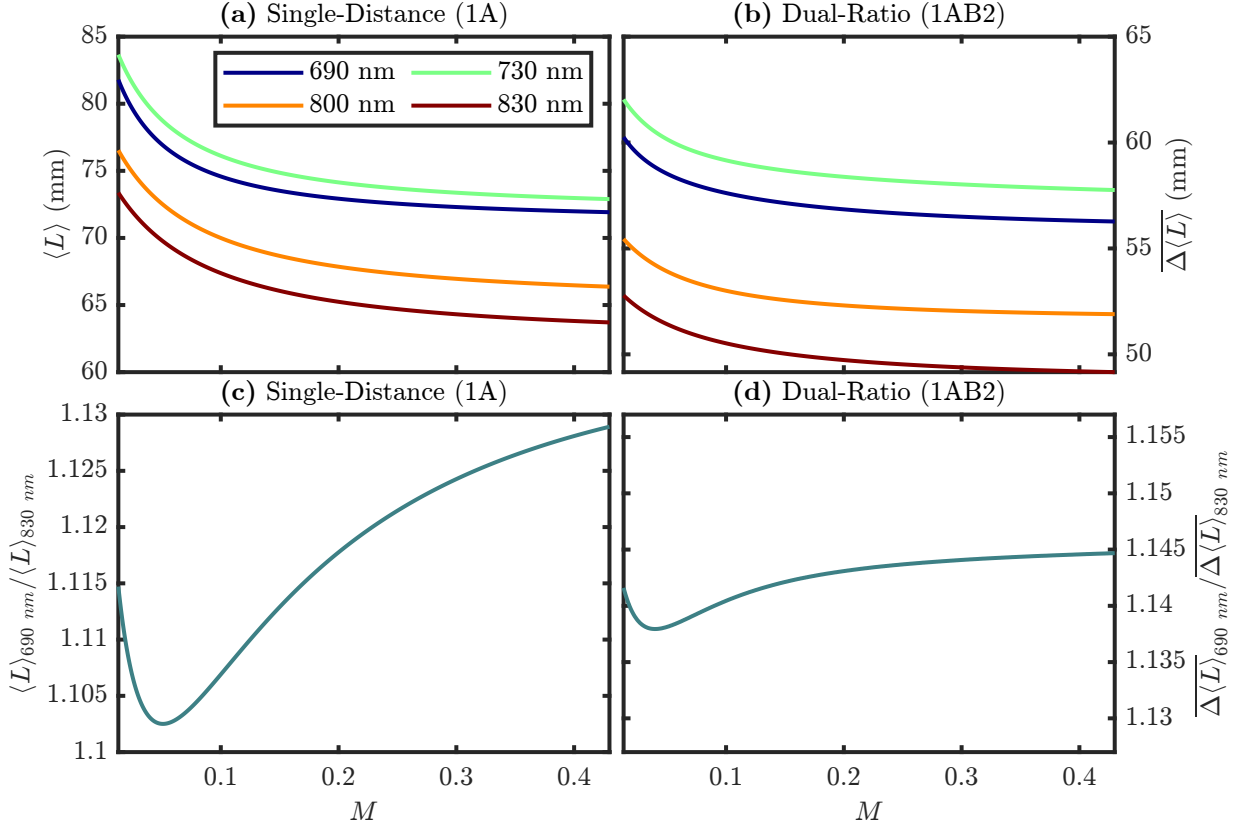


**Fig 4** Monte Carlo (MC) derived average total optical path-lengths ( $\langle L \rangle$ s) and average difference in total optical path-lengths ( $\overline{\Delta \langle L \rangle}$ s) for different optical wavelengths ( $\lambda$ s) as a function of volume fraction of Melanosomes ( $[M]$ ). Also see Table 4. (a)  $\langle L \rangle$  for the Single-Distance (SD) pair formed by source 1 and detector A (Figure 2). (b)  $\overline{\Delta \langle L \rangle}$  for the Dual-Ratio (DR) set (Figure 2; Equation 6). (c) Ratio of  $\langle L \rangle$  at 690 nm over  $\langle L \rangle$  at 830 nm. (d) Ratio of  $\overline{\Delta \langle L \rangle}$  at 690 nm over  $\overline{\Delta \langle L \rangle}$  at 830 nm.

Note: Subplots (c) & (d) are on the same scale but not the same range.

of  $\langle L \rangle$  or  $\overline{\Delta \langle L \rangle}$  between 690 nm and 830 nm is plotted. In the case of  $\langle L \rangle$ , this ratio would be proportional to the calibration factor applied in traditional  $\text{SpO}_2$  measurements. This is because traditional  $\text{SpO}_2$  uses the ratio of the normalized pulsatile amplitude at red and infrared wavelengths.<sup>3</sup> Here, we can also compare how much these ratios change from low to high  $[M]$ . The ratio of  $\langle L \rangle$ s changes from 1.11 to 1.13 for  $[M] = 0.013$  to  $[M] = 0.430$ , respectively; while the ratio of  $\overline{\Delta \langle L \rangle}$ s changes from 1.142 to 1.145 in the same range of  $[M]$ . This is a change of 1.3% for the ratio of  $\langle L \rangle$  and a change of 0.27% for  $\overline{\Delta \langle L \rangle}$ . This suggests that the calibration factor for DR measurements would likely be less sensitive to  $[M]$  than the factor for SD measurements. However, in either case these results suggest that these calibration factors change only by a few percent across  $[M]$  values.

Figure 5 shows the  $\mathcal{S}$  in different tissue regions for various values of  $[M]$  and for the two measurement types, SD or DR. In general both measurement types have the highest  $\mathcal{S}$  to muscle and lowest  $\mathcal{S}$  to epidermis. Comparing SD and DR we see that DR is less sensitive to dynamics in superficial tissues such as dermis and epidermis but more sensitive to dynamics in deep tissues such as muscle when compared to SD. Additionally, looking at the dependence on  $[M]$ , we see that

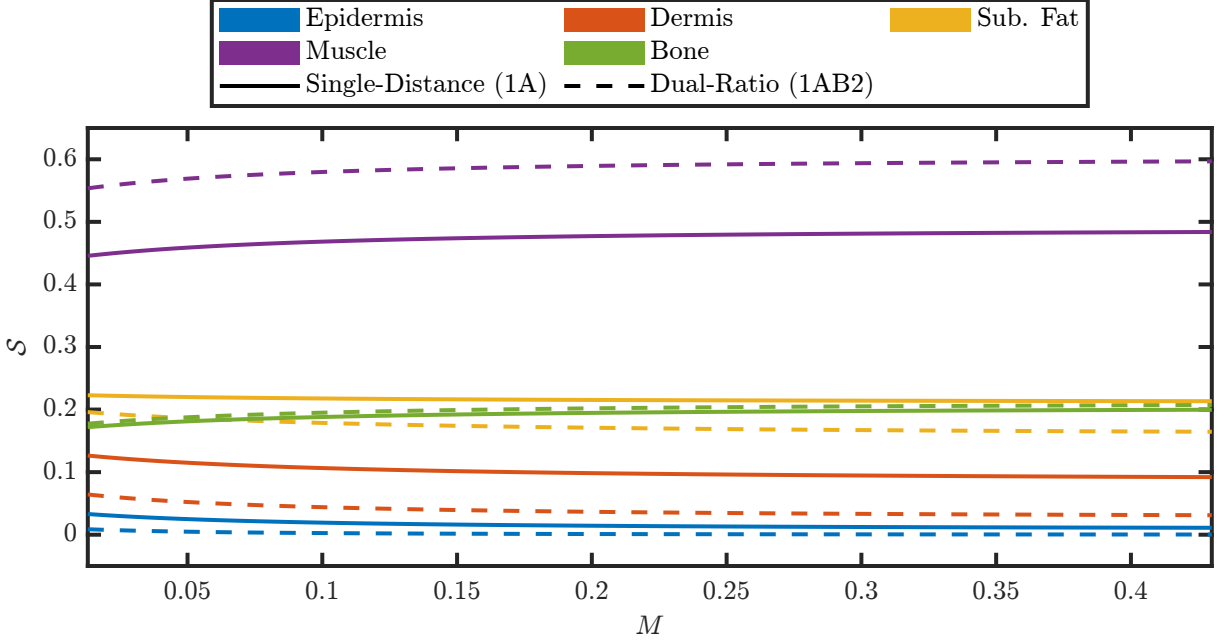


**Fig 5** The Sensitivity to local absorption change ( $\mathcal{S}$ ) at 800 nm for the five different modeled tissues (Figure 2) as a function of volume fraction of Melanosomes ( $[M]$ ). Solid lines show the  $\mathcal{S}$  for the Single-Distance (SD) measurement type and dashed lines for Dual-Ratio (DR) measurement type .

Sensitivity to local absorption change ( $\mathcal{S}$ ) is lost in superficial tissues while deep tissues gain  $\mathcal{S}$  at higher  $[M]$  values. However, these dependencies on  $[M]$  are weak with only a change of a few percent across the full range of  $[M]$  values considered.

Lastly, for this section we shall look at Figure 6 which contains the spatial  $\mathcal{S}$  maps for the two measurement types (*i.e.*, SD and DR) and two volume fraction of Melanosomes ( $[M]$ ) values of 0.013 and 0.430. In general these  $\mathcal{S}$  maps show a similar story to that of Figure 5, with higher values of  $[M]$  resulting in a decrease in superficial  $\mathcal{S}$  and a increase in deep or centralized  $\mathcal{S}$ . We can also look at the  $\mathcal{S}$  very close to the optodes in Figure 6(e),(f),(k),&(l). As seen between Figure 6(e)&(f) there is a reduction of  $\mathcal{S}$  to the epidermis when a high  $[M]$  is considered, which results in a deepening of the bulb of high  $\mathcal{S}$  beneath the optodes for SD measurements. However in Figure 6(k)&(l) we see little to no  $\mathcal{S}$  to superficial tissue for the DR measurement type regardless of  $[M]$ . Note that Figure 6(k)&(l) show black iso-lines which have a speckled nature, which is because many values in the zoomed map are near-zero and noise in the MC is beginning to influence the iso-line shape.

In summary, both Figure 5 and Figure 6 help inform where the measurements of effective  $\Delta\mu_a$  come from and show that different measurement types (*i.e.*, SD and DR), have different sensitivities to different tissue regions. Therefore, if tissue hemodynamics are heterogeneous the partial volume effect governing the recovery of effective  $\Delta\mu_a$  will result in different recovered hemodynamics for different measurements types. For this reason, in further sections, we consider hemodynamic models that contain different oscillations in different tissues to investigate the effects of this partial volume effect.

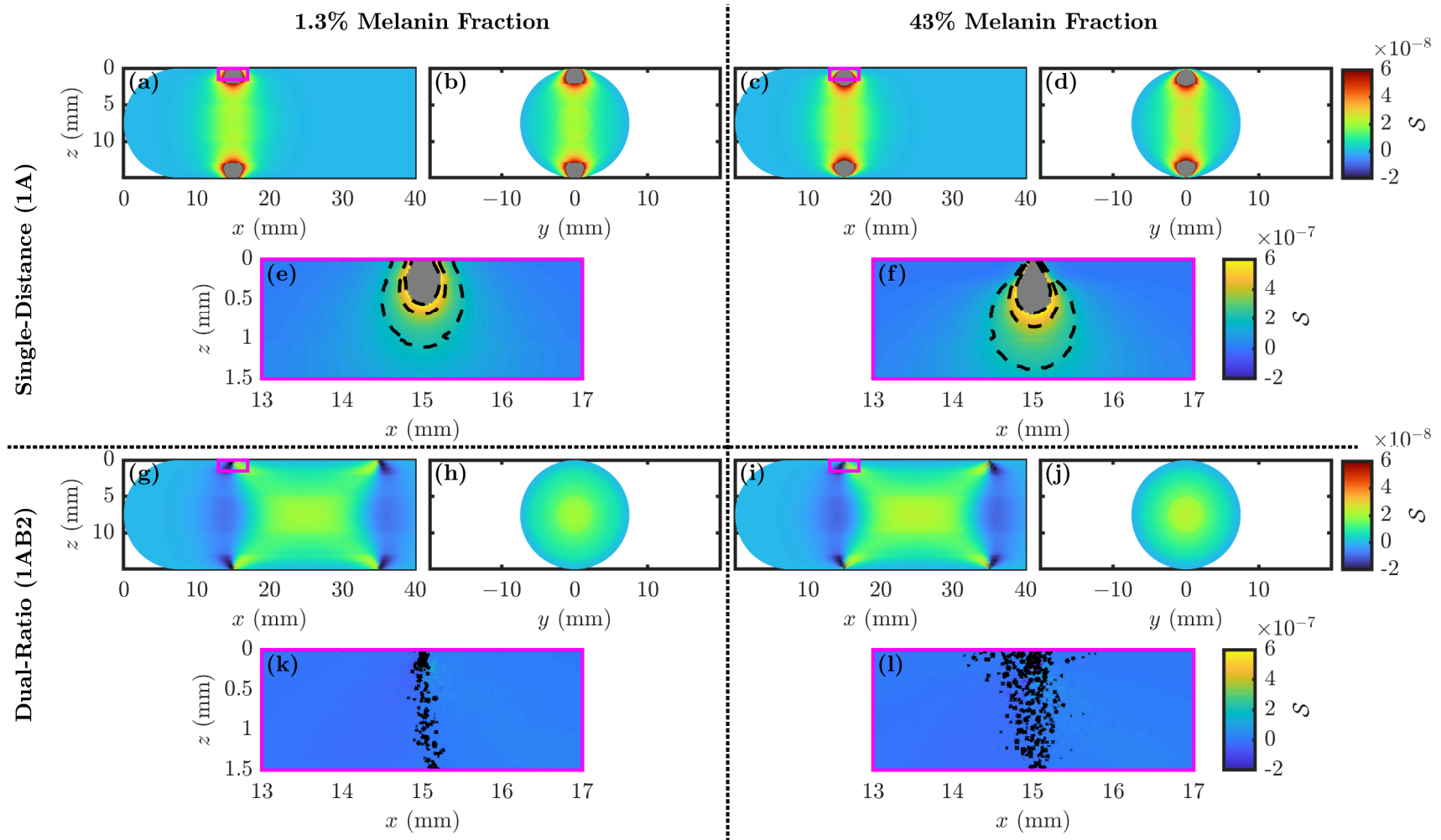


**Fig 6** Spatial maps of the Sensitivity to local absorption change ( $S$ ) at 800 nm for the Single-Distance (SD) ((a)-(f)) or Dual-Ratio (DR) ((g)-(l)) measurement types and volume fraction of Melanosomes ( $[M]$ ) of 0.013 ((a),(b),(e),(g),(h),&(k)) or 0.430 ((c),(d),(f),(i),(j),&(l)). Panels (e),(f),(k),&(l) show a zoomed view of the region indicated by the magenta box in panels (a),(c),(g),&(i), respectively.



### 3.2 Recovered pulsatile saturation from in vivo data

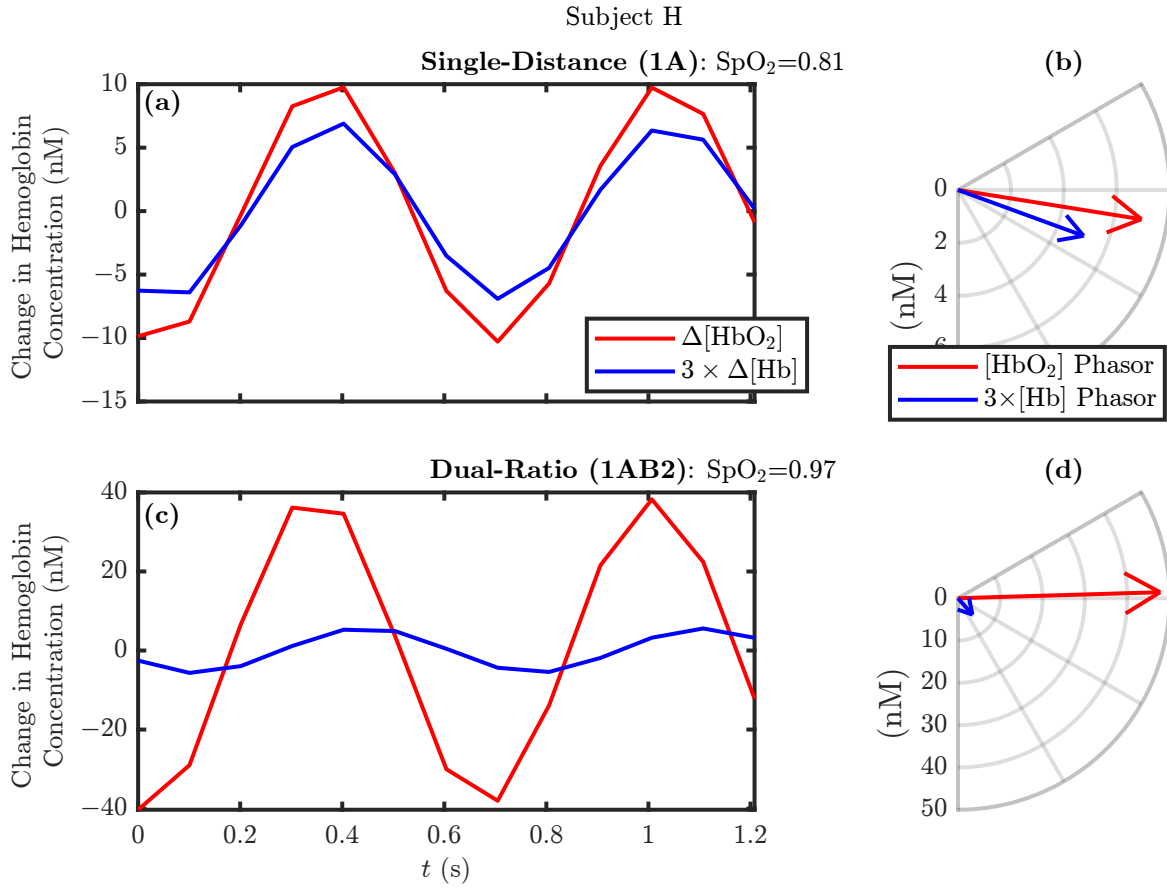


**Fig 7** Example hemodynamics measured by Single-Distance (SD) and Dual-Ratio (DR) for subject H. (a) Folding average for two periods of the band-passed temporal traces of change in Oxy-Hemoglobin concentration ( $\Delta[\text{HbO}_2]$ ) and change in deoxy-Hemoglobin concentration ( $\Delta[\text{Hb}]$ ) measured by SD 1A (Figure 1). (b) Phasors for (a) which have the values:  $[\text{HbO}_2] = (7.0 \angle -9.1^\circ)$  nM and  $[\text{Hb}] = (1.7 \angle -20.1^\circ)$  nM. (c) Same as (a) but measured by DR instead. (d) Phasors for (c) which have the values:  $[\text{HbO}_2] = (48 \angle 1.7^\circ)$  nM and  $[\text{Hb}] = (1.7 \angle -48.6^\circ)$  nM.

Note: The assumed volume fraction of Melanosomes ( $[M]$ ) for this example is 0.013 and the phase reference is  $\Delta[\text{HbO}_2] + \Delta[\text{Hb}]$  measured by DR; see subsection 2.4.1 for further details on analysis.

Note: See footnote i on page 18 regarding recovered pulsatile blood Oxygen Saturation (SpO<sub>2</sub>).

Now we present the results from the *in vivo* experiments. Figure 7 shows example recovered hemodynamic folding average traces and phasors from subject H. Figure 7(a)&(c) contain folding average traces over two periods of the heart-frequency for the band-pass filtered (*i.e.*, with central frequency of the heart-frequency) change in Oxy-Hemoglobin concentration ( $\Delta[\text{HbO}_2]$ ) and change in deoxy-Hemoglobin concentration ( $\Delta[\text{Hb}]$ ) temporal traces from SD and DR measurement types, respectively. While Figure 7(d)&(d) show the corresponding hemodynamic phasors for the oscillations in in Figure 7(a)&(c), respectively. Notice that the amplitudes of these oscillations are on the order of nM due to the small bandwidth of the band-pass filter resulting in little remaining power in the Fourier spectrum.<sup>h</sup>

<sup>h</sup>For comparison the noise floor is on the order of 0.1 nM in the Fourier spectrum making the heart-frequency peak

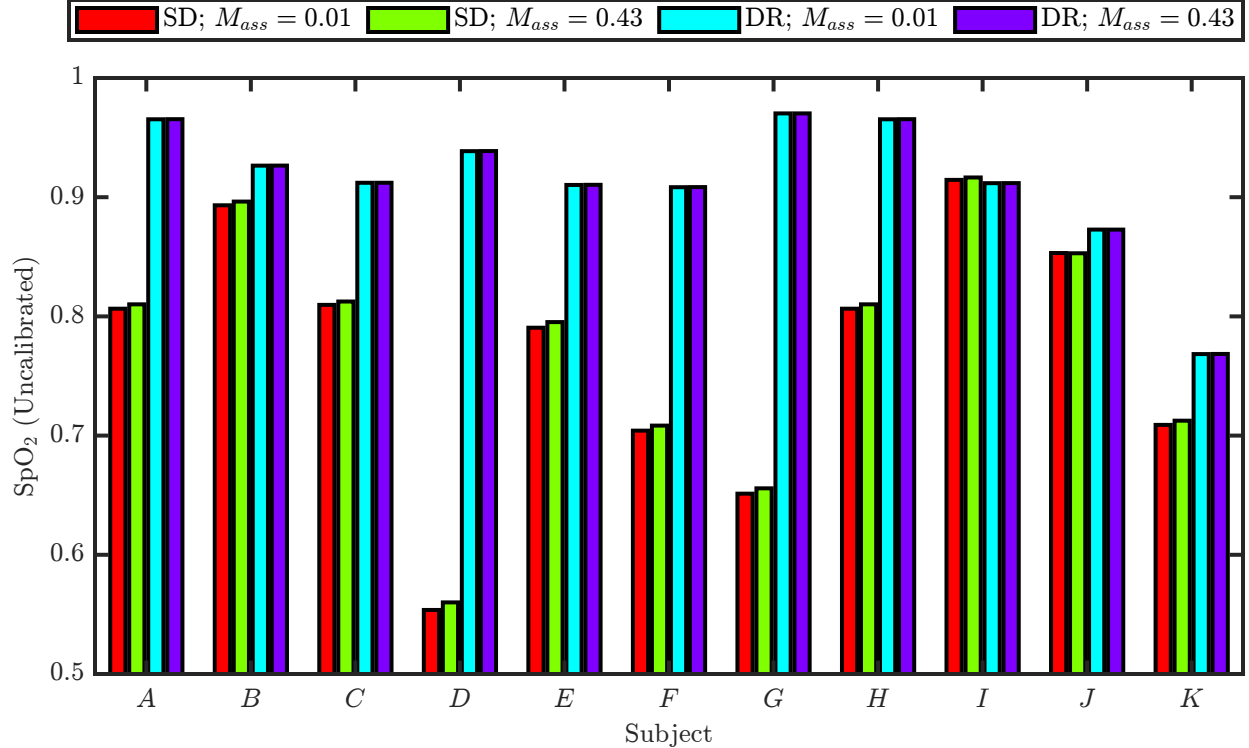


**Fig 8** Recovered pulsatile blood Oxygen Saturation ( $\text{SpO}_2$ )<sup>i</sup> *in vivo* from either Single-Distance (SD) or Dual-Ratio (DR) measurements using an assumed volume fraction of Melanosomes ( $[M]$ ) of 0.013 or 0.430. Subjects are ordered from light to dark skin tones according to [subsubsection 2.4.2](#) & [Figure 3](#).

In this work we do not consider the phase relationship of  $\Delta[\text{HbO}_2]$  and  $\Delta[\text{Hb}]$  when calculating  $\text{SpO}_2$ . However, we show the phasors including their phase relationship in [Figure 7](#) to enable discussion of this consideration and possible future work since it is not considered in [Equation 14](#). Continuing to consider the example in [Figure 7](#), for subject H we see the  $\text{SpO}_2$  recovered from DR was 97% while from SD it was 81%.<sup>i</sup> A further observation is that for both SD and DR the deoxy-Hemoglobin concentration ( $[\text{Hb}]$ ) phasor has a more negative phase relative to the Oxy-Hemoglobin concentration ( $[\text{HbO}_2]$ ) phasor. This may suggest that the true tissue hemodynamics are a mixture of Blood-Volume (BV) (*i.e.*, in-phase) and Blood-Flow (BF) (*i.e.*, out-of-phase) oscillations at the heart-frequency, not solely BV oscillations as is required for  $\text{SpO}_2$  measurements.

We now move from the example data set in [Figure 7](#) to a summary of the recovered  $\text{SpO}_2$  for all subjects in [Figure 8](#). Here, we show the recovered  $\text{SpO}_2$  with SD and DR for assumed  $[M]$  values of 0.013 and 0.430. In all cases, except subject I, the recovered  $\text{SpO}_2$  from DR was higher than the recovered  $\text{SpO}_2$  from SD; for subject I, the recovered  $\text{SpO}_2$  with the two measurement types was close to equal. Furthermore, examining the dependence on the assumed value of  $[M]$  we see that a higher  $[M]$  increases the recovered  $\text{SpO}_2$  for SD by a small amount; on the order of 0.5%. While it has no noticeable effect on the recovered  $\text{SpO}_2$  with DR. Since [Figure 8](#) shows no substantial

<sup>i</sup>Signal-to-Noise Ratio (SNR) on the order of 10.

<sup>i</sup>We consider these  $\text{SpO}_2$  measurements uncalibrated since they do not represent  $\text{SaO}_2$  due to different partial volume effects, typical  $\text{SpO}_2$  techniques would effectively apply a calibration factor to these values to recover a  $\text{SaO}_2$  surrogate.

difference between the  $\text{SpO}_2$  recovered using different assumed values of  $[\text{M}]$ , the assumed values of  $[\text{M}]$  have little impact for the analysis methods presented here (subsubsection 2.4.1), especially in the case of DR.

We may also examine Figure 8 in terms of skin tone dependence. As a reminder, we have ordered the subjects A to K in order from lightest to darkest skin tone according to the methods in subsubsection 2.4.2 and Figure 3. The SD measurements appear to have little to no dependence on skin tone, though the values of recovered  $\text{SpO}_2$  vary greatly with a minimum of 55 % for subject D to a maximum of 91 % for subject I. By contrast, the variation of recovered  $\text{SpO}_2$  values for DR across subjects is much less, with a minimum of 77 % for subject k and a maximum of 97 % for subject G. We also point out that Figure 8 may show a dependence on skin tone for DR measurements if we look at the recovered  $\text{SpO}_2$  values from subject H to subject K. This may suggest an affect that results in a lower recovered  $\text{SpO}_2$  for darker skin when using DR. This would represent a negative bias which is at odds with results for conventional pulse-oximetry in the literature.<sup>14,15</sup> These lower  $\text{SpO}_2$ s recovered by DR, particularly for subjects J and K, aren't corrected for by assuming relevant  $[\text{M}]$  (*i.e.*, there is no noticeable difference between assuming  $[\text{M}]$  of 0.013 or 0.430 for any subject). We caution that this dependence observed in subjects H to K is tenuous due to the small number of subjects and the observed variations in  $\text{SpO}_2$  across all subjects. We only point out this dependence as a possible point of discussion that will be further investigated in future work, which will also consider the phase differences between  $\Delta[\text{HbO}_2]$  and  $\Delta[\text{Hb}]$  (Figure 7).

### 3.3 Recovered saturation from Monte-Carlo simulations informed by *in vivo* results

As described in subsubsection 2.3.3, we may simulate either SD or DR measurements for different tissue hemodynamics and  $[\text{M}]$  values based on the MC model. Furthermore, we can simulate measurements for given hemodynamics and a value for  $[\text{M}]$  but analyze the data with a different assumed value of  $[\text{M}]$  to investigate the effect of such assumption. Of course, these simulations are with the caveat of being within the context of the MC finger model in this work.

One consistent result of the *in vivo* measurements reported in Figure 8 was that  $\text{SpO}_2$  recovered by DR was greater than the one recovered by SD. This may be explained by different hemodynamics in different tissues where SD and DR have different Sensitivity to local absorption change ( $S$ ) making the partial volume effect come into play (Figure 5 and Figure 6). We report a simulation of hemodynamic phasors at the heart-frequency that recreate this consistent result. To that end, we may model hemodynamics as combinations of BV and BF, with  $[\text{HbO}_2]$  and  $[\text{Hb}]$  phasors being in-phase if driven by BV oscillations and out-of-phase if driven by BF oscillations. Further, the relative amplitudes of the arterial BV components of the  $[\text{HbO}_2]$  and  $[\text{Hb}]$  phasors is  $\text{SaO}_2$ . For BF components, the amplitudes of  $[\text{HbO}_2]$  and  $[\text{Hb}]$  phasors are equal. Considering this, we modeled hemodynamics as a combination of BF and BV with an  $\text{SaO}_2$  of 95 %. Oscillations were assumed to be in the dermis and muscle only, with only the dermis having a BF contribution. In the dermis the BF components were  $(1\angle 135^\circ)$   $\mu\text{M}$  for the  $[\text{HbO}_2]$  phasor and  $(1\angle -45^\circ)$   $\mu\text{M}$  for the  $[\text{Hb}]$  phasor, while BV components were  $(2.85\angle 0^\circ)$   $\mu\text{M}$  for the  $[\text{HbO}_2]$  phasor and  $(0.15\angle 0^\circ)$   $\mu\text{M}$  for the  $[\text{Hb}]$  phasor (Figure 9(a)). Meanwhile, for the muscle, the BV components were  $(1.90\angle 0^\circ)$   $\mu\text{M}$  for the  $[\text{HbO}_2]$  phasor and  $(0.10\angle 0^\circ)$   $\mu\text{M}$  for the  $[\text{Hb}]$  phasor (Figure 9(c)). Given this simulation and the model, the recovered phasors are shown in Figure 9(b)&(d) which recreate the greater  $\text{SpO}_2$  recovered by DR which was observed *in vivo*. We also note that the simulation in Figure 9

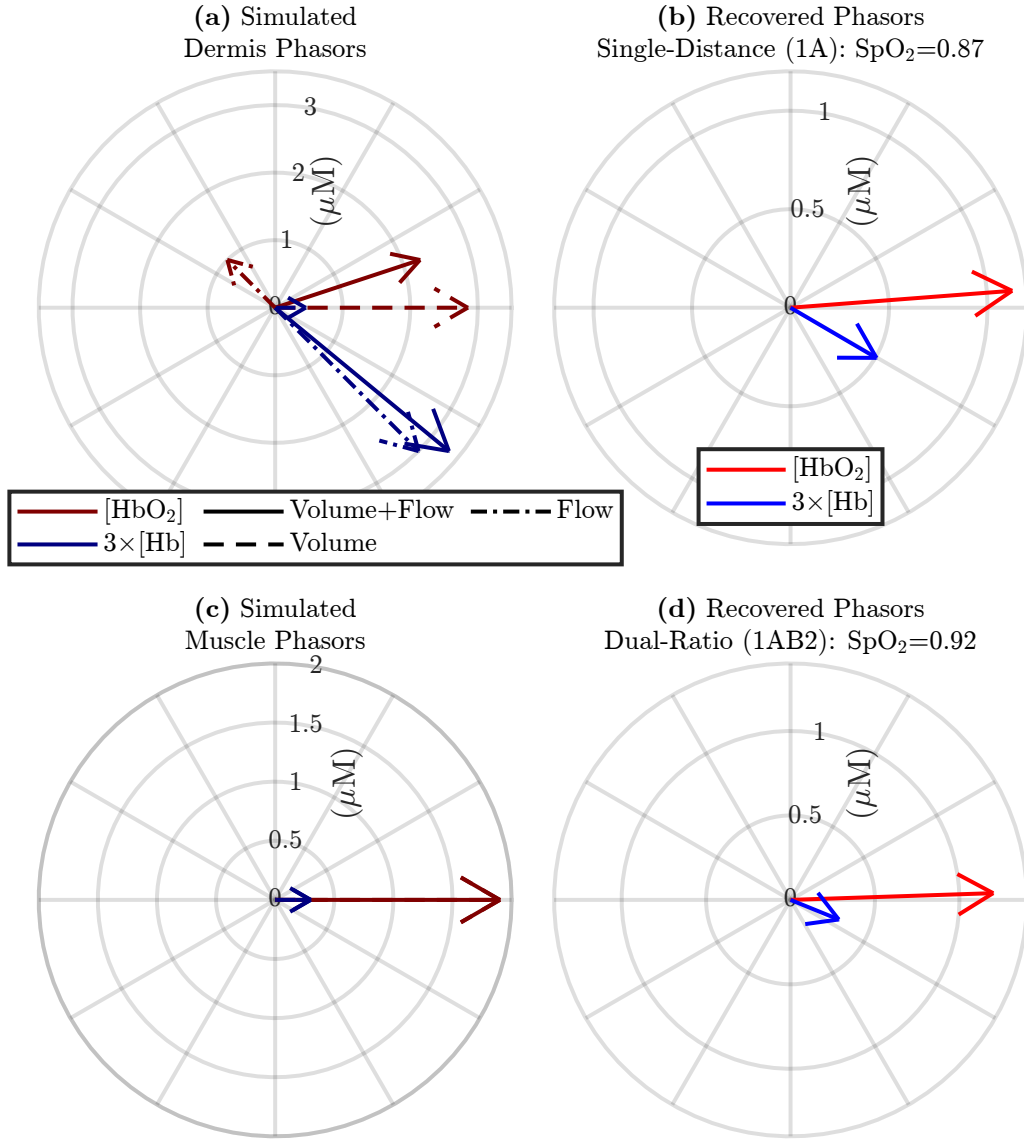


**Fig 9** Simulation of tissue Oxy-Hemoglobin concentration ( $[\text{HbO}_2]$ ) and deoxy-Hemoglobin concentration ( $[\text{Hb}]$ ) phasors leading to recovered phasors and pulsatile blood Oxygen Saturation ( $\text{SpO}_2$ ) measured by Single-Distance (SD) or Dual-Ratio (DR). Hemodynamics are only in the dermis (Blood-Volume (BV) and Blood-Flow (BF)) and muscle (only BV). BV oscillations have a saturation of 95%. Volume fraction of Melanosomes ( $[\text{M}]$ ) modeled as 0.013. (a) Dermis phasors:  $(2.26 \angle 18.3^\circ) \mu\text{M}$  for  $[\text{HbO}_2]$  and  $(1.11 \angle -39.5^\circ) \mu\text{M}$  for  $[\text{Hb}]$ . (b) SD recovered phasors:  $(1.13 \angle 4.4^\circ) \mu\text{M}$  for  $[\text{HbO}_2]$  and  $(0.17 \angle -30.3^\circ) \mu\text{M}$  for  $[\text{Hb}]$ . (c) Muscle phasors:  $(1.90 \angle 0^\circ) \mu\text{M}$  for  $[\text{HbO}_2]$  and  $(0.10 \angle 0^\circ) \mu\text{M}$  for  $[\text{Hb}]$ . (d) DR recovered phasors:  $(1.20 \angle 1.9^\circ) \mu\text{M}$  for  $[\text{HbO}_2]$  and  $(0.10 \angle -22.1^\circ) \mu\text{M}$  for  $[\text{Hb}]$ .

qualitatively recreates the phase relationships between  $[\text{HbO}_2]$  and  $[\text{Hb}]$  phasors shown in the example dataset in Figure 7, though we do not put much weight on this agreement since it is with one example subject.

We can extend these simulations by investigating the assumed value of  $[\text{M}]$  for  $\text{SpO}_2$ . For this,

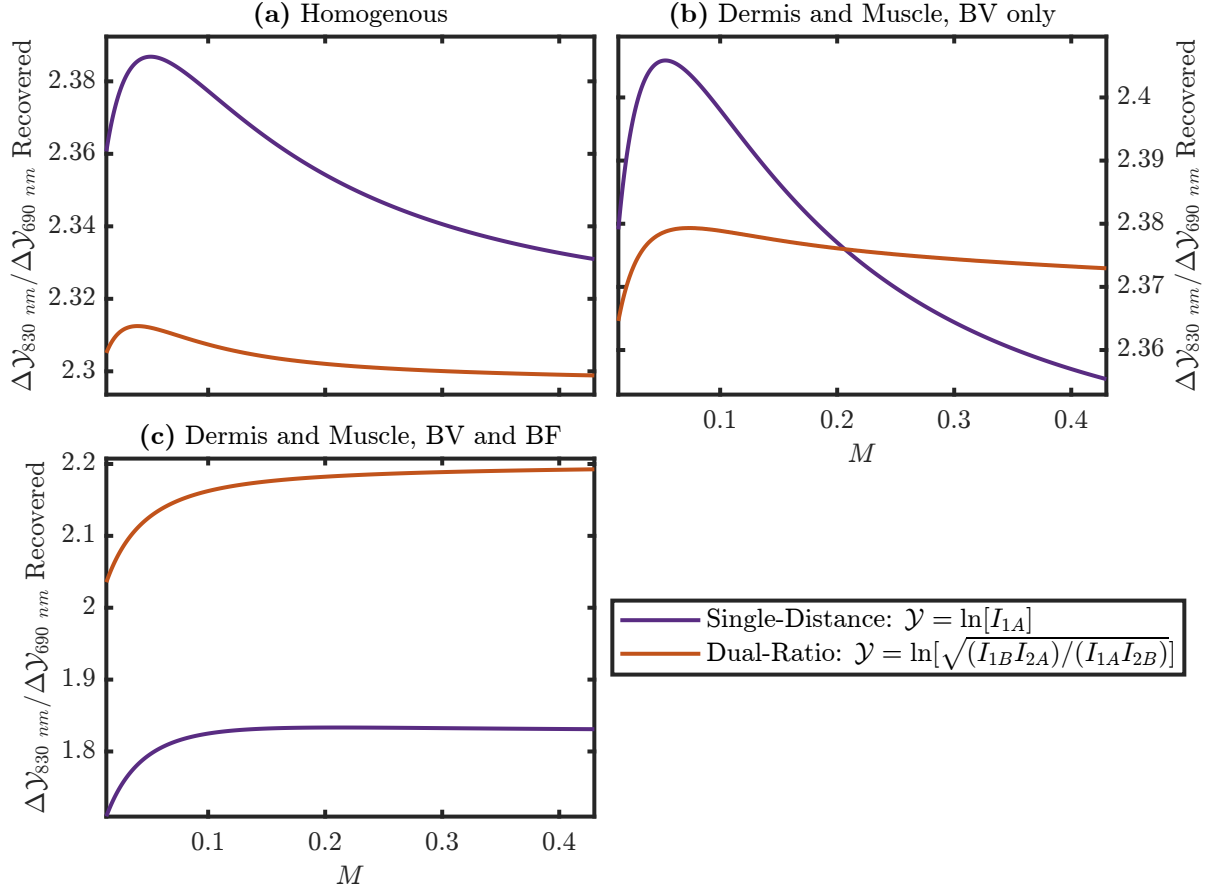


**Fig 10** Simulated ratios of the changes in optical data ( $\mathcal{Y}$ ) at 830 nm and 690 nm as a function of modeled  $[M]$ . Changes in  $\mathcal{Y}$  are the numerators of Equation 1 or Equation 2 which are also written in the legend for either Single-Distance (SD) or Dual-Ratio (DR). (a) Simulation with homogeneous Blood-Volume (BV) oscillations in the whole tissue with phasor values of  $(0.95\angle 0^\circ)$   $\mu\text{M}$  for Oxy-Hemoglobin concentration ( $[\text{HbO}_2]$ ) and  $(0.05\angle 0^\circ)$   $\mu\text{M}$  for deoxy-Hemoglobin concentration ( $[\text{Hb}]$ ). (b) Simulation with BV oscillations only in the dermis and muscle again with phasor values of  $(0.95\angle 0^\circ)$   $\mu\text{M}$  for  $[\text{HbO}_2]$  and  $(0.05\angle 0^\circ)$   $\mu\text{M}$  for  $[\text{Hb}]$ . (c) Simulation with Blood-Flow (BF) and BV oscillations in the dermis and only BV in the muscle. This is the same simulation as Figure 9, and the simulated phasor values may be found there.

we consider three different hemodynamic simulations (*i.e.*, two simulations in addition to the one already described). One hemodynamic simulation is the one in Figure 9 which recreated some aspects of the *in vivo* results and considers a simulation of BV and BF in the dermis and only BV in the muscle. The first additional simulation assumed a homogeneous BV oscillation and  $\text{SaO}_2$  of 0.95 % in all tissues, with no BF oscillations anywhere. That is an  $[\text{HbO}_2]$  phasor of  $(0.95\angle 0^\circ)$   $\mu\text{M}$  and an  $[\text{Hb}]$  phasor of  $(0.05\angle 0^\circ)$   $\mu\text{M}$  in all tissues. This homogeneous case will only show the effect of different assumed values of  $[M]$ . The second additional simulation is similar to the first, with only BV oscillations, but now only in the dermis and muscle and no hemodynamics at the heart-frequency in the other tissues. This case also considered an  $[\text{HbO}_2]$  phasor of  $(0.95\angle 0^\circ)$   $\mu\text{M}$  and an  $[\text{Hb}]$  phasor of  $(0.05\angle 0^\circ)$   $\mu\text{M}$ , but now only in the dermis and muscle.

Figure 10 shows simulated recovered data for the three hemodynamic simulations presented in

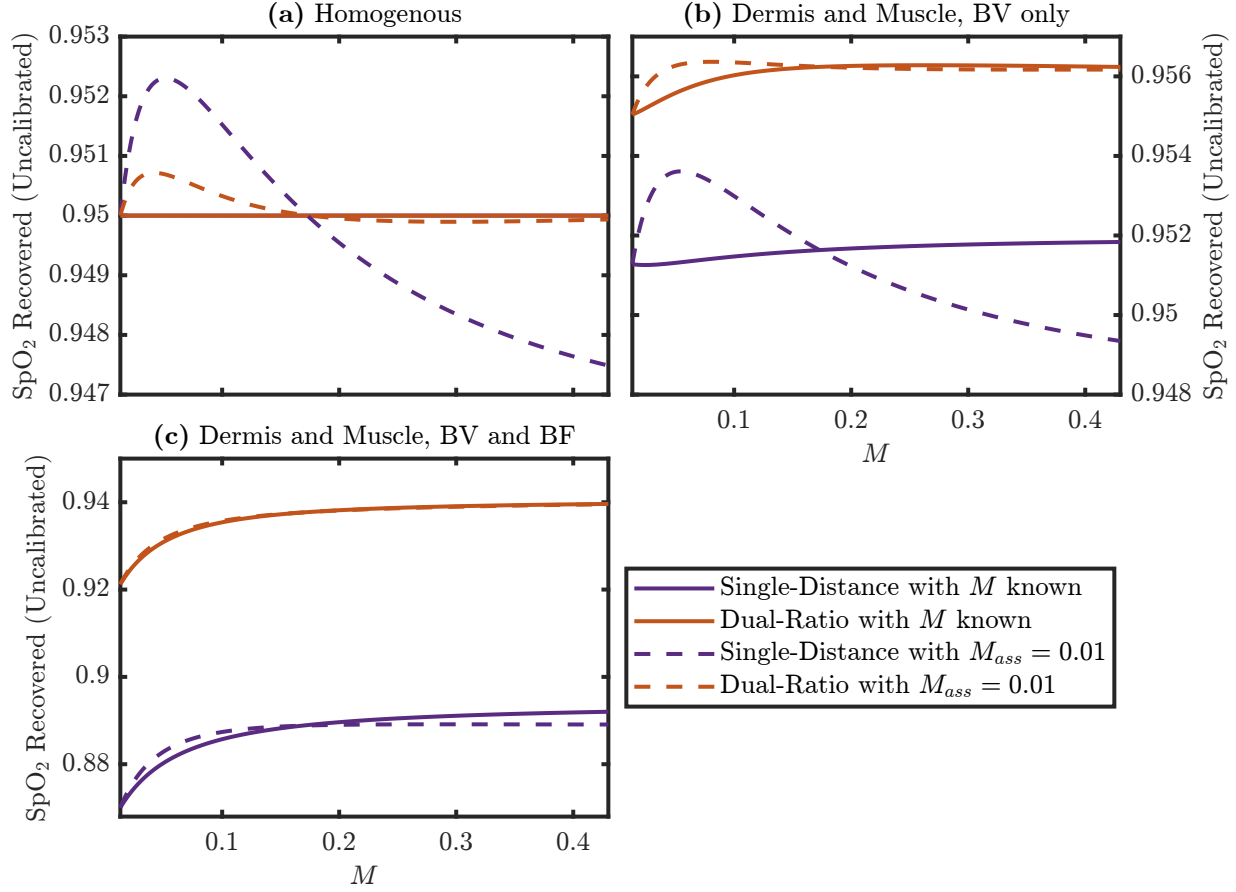


**Fig 11** Simulated recovered pulsatile blood Oxygen Saturation ( $\text{SpO}_2$ ) for Single-Distance (SD) or Dual-Ratio (DR). Solid lines are the case where the true volume fraction of Melanosomes ( $[M]$ ) is known and used to recover  $\text{SpO}_2$ , while dashed lines assume a value for  $[M]$  of 0.013. For all simulations the true arterial blood Oxygen Saturation ( $\text{SaO}_2$ ) from Blood-Volume (BV) oscillations is 95%. (a) Simulation with homogeneous BV oscillations in the whole tissue with phasor values of  $(0.95\angle 0^\circ)$   $\mu\text{M}$  for Oxy-Hemoglobin concentration ( $[\text{HbO}_2]$ ) and  $(0.05\angle 0^\circ)$   $\mu\text{M}$  for deoxy-Hemoglobin concentration ( $[\text{Hb}]$ ). (b) Simulation with BV oscillations only in the dermis and muscle again with phasor values of  $(0.95\angle 0^\circ)$   $\mu\text{M}$  for  $[\text{HbO}_2]$  and  $(0.05\angle 0^\circ)$   $\mu\text{M}$  for  $[\text{Hb}]$ . (c) Simulation with Blood-Flow (BF) and BV oscillations in the dermis and only BV in the muscle. This is the same simulation as [Figure 9](#), and the simulated phasor values may be found there.

a similar way to the data collected for traditional  $\text{SpO}_2$  methods, as ratios of pulsatile components of  $\Delta\mathcal{Y}$  at two wavelengths. In [Figure 10](#) the ratio of changes in  $\Delta\mathcal{Y}$  at 830 nm and 690 nm are plotted versus  $[M]$ . For SD and DR changes in  $\Delta\mathcal{Y}$  is given by the numerators of the right-hand-side of [Equation 1](#) and [Equation 2](#), respectively. The three panels of [Figure 10](#) represent the three simulations. One will note that, the recovered data for both SD and DR does depend on  $[M]$ , but the dependence on  $[M]$  is stronger for SD in the two simulations which assume no BF oscillations (*i.e.*, the first and second).

Finally, we come to [Figure 11](#) which conveys the same information as [Figure 10](#) but with the added information of what the recovered  $\text{SpO}_2$  would be for different cases of assumed  $[M]$ . [Figure 11](#) considers all four wavelengths but [Figure 10](#) only considers 690 nm and 830 nm. The

three simulations described above are shown in Figure 11, and the dashed lines represent simulated data analyzed with an assumed  $[M]$  of 0.013. In all three simulations the true  $SaO_2$  (*i.e.*, the saturation of the BV oscillation) is 95%. The true  $[M]$  in the simulation (*i.e.*, the one used to generate the forward data) corresponds to the value on the  $x$ -axis and solid lines are recovered  $SpO_2$  using this true  $[M]$  value. First, let's look at Figure 11(a) which shows the simulation with homogeneous BV oscillations in all the tissue regions. The solid lines in Figure 11(a) match the simulated  $SaO_2$  and recover a  $SpO_2$  of 95% which verifies the validity of the methods in this work. Note that the solid lines in Figure 11(a) are coincident. Further the deviation of the dashed line from the solid line shows the effect of assuming an incorrect value of  $[M]$  without any partial-volume effects confounding the simulation. From this we see that the recovered  $SpO_2$  from SD deviates from the true value by less than 0.25%, while the recovered  $SpO_2$  from DR deviates by less than 0.1%. Moving to the second simulation in Figure 11(b), which only considers BV oscillations that are in the dermis and muscle, we see a similar story to Figure 11(a) but with a systematic shift for the SD or DR recovered  $SpO_2$ . In both cases  $SpO_2$  overestimates the simulated  $SaO_2$ , with DR overestimating it more, with the difference at about 0.6%. These shifts of the solid lines in Figure 11(b) results from partial volume effects. Finally, we move to the last simulation in Figure 11(c), which is the same as Figure 9. In this case, there is a large difference between  $SpO_2$  recovered by SD and DR. This result matches the *in vivo* data in that the value for DR is greater regardless of  $[M]$ . Additionally, the recovered  $SpO_2$  varies by about 2% across  $[M]$  for both measurement types and this is not corrected for by knowing the true  $[M]$  when analyzing the data (*i.e.*, the solid curve varies more than the difference between the solid and dashed curves). Since the recovered  $SpO_2$  in Figure 11(c) increases with increasing  $[M]$ , this is at odds with the decrease observed between subjects H and K as shown in Figure 8, further suggesting that this observation from Figure 8 may not be significant.

Wrapping up these simulations, we can see that the partial volume effect and heterogeneous tissue hemodynamic phasors affect  $SpO_2$  values recovered by both SD and DR to a greater extent than different values of  $[M]$ , whether or not the correct value of  $[M]$  is known. Furthermore, in the simulation which roughly recreated the *in vivo* results (Figure 11(c)) DR recovered a  $SpO_2$  value closer to the modeled  $SaO_2$ . This is consistent with the higher values of  $SpO_2$  found by DR in the *in vivo* data presented in Figure 8. But these trends in Figure 11 show changes in recovered  $SpO_2$  that are much less than the observed differences in recovered  $SpO_2$  between different subjects in Figure 8. These greater differences *in vivo* suggest that the simulations may not be capturing the full picture. We conclude this section by reminding the readers that these results are all within the context of the MC model we used in this work, which assumes a particular anatomy, optical properties, and model of skin tone based on  $[M]$ .

## 4 Discussion

In this work, we presented a Monte Carlo (MC) model to simulate optical measurements on the human finger and experimental results obtained *in vivo* using the same optical measurement geometry (Figure 1). We designed the finger MC model based on a simplified geometry of tissue types in a human finger and assumed optical properties based on previous literature.<sup>25,26</sup> Then we utilized this model to analyze the *in vivo* data and recover  $SpO_2$  for two different measurement types (*i.e.*, Single-Distance (SD) and Dual-Ratio (DR)). The results of the *in vivo* experiment were

then used to inform models of hemodynamic oscillations and enable a discussion of the differences between measurement types, assumed  $[M]$ , and heterogeneous tissue hemodynamics.

The MC simulations culminated in the results of [Figure 11](#) for three different tissue hemodynamic models. These models considered hemodynamic oscillations at the heart-frequency in different tissue regions with different phase and amplitude relationships. One hemodynamic model was created to roughly match some consistent results obtained in the *in vivo* measurements. In contrast, two other hemodynamic models were used to investigate the interplay between tissue hemodynamic heterogeneity and assumed values of  $[M]$ . Overall, the results showed that the assumed value for  $[M]$ , whether assumed incorrectly or correctly, affected the recovered  $\text{SpO}_2$  on the order of 1 %. However, the modeled heterogeneity of tissue hemodynamics significantly affected the recovered  $\text{SpO}_2$ ; this effect was greater than the effect from assumed  $[M]$ . The different results obtained with different measurement types are due to different partial volume effects and show evidence of spatially heterogeneous tissue hemodynamics.

Expounding upon these ideas regarding assumed values of  $[M]$  or spatially varying tissue hemodynamics, we can focus on [Figure 4](#), [Figure 10](#), and [Figure 11](#). [Figure 4](#) represents the proportionality constants modeled by the MC simulations, which govern how the change in the measured optical data are converted to the  $\Delta\mu_a$ , which would later be converted to the change in Oxy-Hemoglobin concentration ( $\Delta[\text{HbO}_2]$ ) and change in deoxy-Hemoglobin concentration ( $\Delta[\text{Hb}]$ ), and then finally  $\text{SpO}_2$ . The simulations reported in [Figure 10](#) show that the measured optical data are affected by different hemodynamic situations and  $[M]$  values. Finally, [Figure 11](#) shows the simulated recovered  $\text{SpO}_2$  for the same hemodynamic situations as in [Figure 10](#). The lines in [Figure 11](#) effectively result from a multiplication of the values in [Figure 4\(c\)&\(d\)](#) and [Figure 10](#).<sup>j</sup> This relationship, between the values of [Figure 4](#), [Figure 10](#), and [Figure 11](#), shows the interplay between the measured optical data and assumed calibration constants needed to obtain  $\Delta\mu_a$ , which is related to  $\text{SpO}_2$  through known extinction coefficients.<sup>23</sup> Effectively, the curves in [Figure 4\(c\)&\(d\)](#) are the calibration constants that would need to be found to convert optical data to a measurement proportional to  $\text{SpO}_2$  and therefore their variation over  $[M]$  shows how these calibration constants may need to change with skin tone. Meanwhile, [Figure 10](#) and [Figure 11](#) add the consideration of heterogeneous tissue hemodynamic oscillations and how the recovered measurements would change with them.

Looking at all of these together, we see that the recovered  $\text{SpO}_2$  was more influenced by hemodynamic heterogeneity than assumed  $[M]$ . Since different people will likely have different hemodynamic heterogeneity we will expect that the recovered  $\text{SpO}_2$  will vary more across subjects than across assumed  $[M]$  values within a subject. This is in-fact observed in [Figure 8](#) where variation across subject is much greater than the differences obtained by assuming different  $[M]$  values. Furthermore, the variation across subjects is greater for SD compared to DR suggesting that DR, at least in-part, compensates for the subject differences. We can put these results in the context of [Reference 15](#) which showed a bias in the  $\text{SpO}_2$  measured on Black versus White patients. In [Reference 15](#) the variation across patients (*i.e.*, for a given value of  $\text{SaO}_2$ ) was greater than the observed skin tone bias. This skin tone bias, in [Reference 15](#), is evident when considering the large patient population which, when averaged, likely suppressed the hemodynamic or physiological differences between the patients making the effect of skin tone appear. Our results are in-line

---

<sup>j</sup>This statement is not formally true since [Figure 4\(c\)&\(d\)](#) and [Figure 10](#) consider two wavelengths but [Figure 11](#) uses all four wavelengths in this work.



with this interpretation of the results in Reference 15 given that we expect more variation in  $\text{SpO}_2$  from hemodynamic differences than skin tone (*i.e.*, modeled as  $[M]$ ) differences.

One criticism of traditional  $\text{SpO}_2$  measurements is that the calibration factor is assumed to be the same for all skin tones and thus  $[M]$ .<sup>7,17</sup> For the results obtained from the models, simulations, and analysis methods reported in this article, we see that this assumption creates only small inaccuracies in  $\text{SpO}_2$ , on the order of 1%. Instead, the results in this work show that the larger confound on recovered  $\text{SpO}_2$  measurements is the heterogeneity of tissue hemodynamics.

Beyond the discussion of  $[M]$  and tissue heterogeneity, we also explore the difference between measurement types, SD and DR. One consistent result that we see from the *in vivo* data was a higher  $\text{SpO}_2$  recovered by DR compared to SD. More importantly, the  $\text{SpO}_2$  recovered by DR was more consistent across these healthy human subjects, which is consistent with these subjects having approximately the same nominal  $\text{SaO}_2$ . This result was recreated in a simulation that modeled pulsatile Blood-Volume (BV) in the dermis and muscle tissue, with pulsatile Blood-Flow (BF) in only occurring in the dermis. However, the hemodynamic model and relationship of tissue sensitivities are complex, so we do not claim that this simulation, which recreated the *in vivo* data relationships, is necessarily representative of the actual tissue dynamics. While this case may be possible, other situations may also reproduce our *in vivo* results.

## 5 Conclusion

In conclusion, our results indicate that optical measurements of  $\text{SpO}_2$  may be more dependent on heterogeneity in tissue hemodynamics than on the assumed value of  $[M]$ . Furthermore, we found that Dual-Ratio (DR) measurements recovered greater and more consistent  $\text{SpO}_2$  values than Single-Distance (SD) measurements across various subjects. These results will further enable discussions about optimal methods to recover  $\text{SpO}_2$  with minimal impact from skin tone. Further, these results show promise of the DR method for  $\text{SpO}_2$  measurements on the human finger. Future directions include considering the amplitude and phase relationships of pulsatile hemodynamics of change in Oxy-Hemoglobin concentration ( $\Delta[\text{HbO}_2]$ ) and change in deoxy-Hemoglobin concentration ( $\Delta[\text{Hb}]$ ) when measuring  $\text{SpO}_2$ , finding ways to better assess and account for different  $[M]$ s and skin tones, investigating pulsatile hemodynamic heterogeneity in the finger, considering the number and values of wavelengths used, using of novel measurement methods such as DR, and considering time-resolved optical changes in the time or frequency domain. We hope that this work may represent a jumping off point for future work on these considerations.

### *Disclosures*

The authors disclose no conflicts of interest.

### *Data, Materials, and Code Availability*

Applicable supporting code and data are available from the authors upon reasonable request.

## Acknowledgments

This work is supported by National Institutes of Health (NIH) award R01-EB029414. G.B. would also like to acknowledge support from NIH award K12-GM133314. The content is solely the authors' responsibility and does not necessarily represent the official views of the awarding institutions.

We would also like to acknowledge helpful correspondence with Qianqian Fang regarding Monte-Carlo eXtreme.

## References

- 1 K. K. Tremper, "Pulse oximetry," *Chest* **95**(4), 713–715 (1989).
- 2 J. W. Severinghaus, "Takuo Aoyagi: Discovery of Pulse Oximetry," *Anesthesia & Analgesia* **105**, S1 (2007). [https://journals.lww.com/anesthesia-analgesia/fulltext/2007/12001/takuo\\_aoyagi\\_\\_discovery\\_of\\_pulse\\_oximetry.1.aspx](https://journals.lww.com/anesthesia-analgesia/fulltext/2007/12001/takuo_aoyagi__discovery_of_pulse_oximetry.1.aspx).
- 3 M. Nitzan, A. Romem, and R. Koppel, "Pulse oximetry: Fundamentals and technology update," *Medical Devices: Evidence and Research* **7**, 231–239 (2014). <https://www.dovepress.com/pulse-oximetry-fundamentals-and-technology-update-peer-reviewed-fulltext>
- 4 E. D. Chan, M. M. Chan, and M. M. Chan, "Pulse oximetry: Understanding its basic principles facilitates appreciation of its limitations," *Respiratory Medicine* **107**, 789–799 (2013). <https://www.sciencedirect.com/science/article/pii/S095461111300053X>.
- 5 T. Leppänen, S. Kainulainen, H. Korkalainen, *et al.*, "Pulse oximetry: The working principle, signal formation, and applications," in *Advances in the Diagnosis and Treatment of Sleep Apnea: Filling the Gap between Physicians and Engineers*, 205–218, Springer (2022).
- 6 G. A. Millikan, "The Oximeter, an Instrument for Measuring Continuously the Oxygen Saturation of Arterial Blood in Man," *Review of Scientific Instruments* **13**, 434–444 (1942). <https://doi.org/10.1063/1.1769941>.
- 7 K. Setchfield, A. Gorman, A. H. R. W. Simpson, *et al.*, "Effect of skin color on optical properties and the implications for medical optical technologies: A review," *Journal of Biomedical Optics* **29**, 010901 (2024). <https://www.spiedigitallibrary.org/journals/journal-of-biomedical-optics/volume-29/issue-1/010901/Effect-of-skin-color-on-optical-properties-and-the-implications/10.1117/1.JBO.29.1.010901.full>.
- 8 R. Al-Halawani, P. H. Charlton, M. Qassem, *et al.*, "A review of the effect of skin pigmentation on pulse oximeter accuracy," *Physiological Measurement* (2023).
- 9 C. Shi, M. Goodall, J. Dumville, *et al.*, "The accuracy of pulse oximetry in measuring oxygen saturation by levels of skin pigmentation: A systematic review and meta-analysis," *BMC medicine* **20**(1), 267 (2022).
- 10 A. M. Cabanas, M. Fuentes-Guajardo, K. Latorre, *et al.*, "Skin pigmentation influence on pulse oximetry accuracy: A systematic review and bibliometric analysis," *Sensors* **22**(9), 3402 (2022).
- 11 A. Bierman, K. Benner, and M. S. Rea, "Melanin bias in pulse oximetry explained by light source spectral bandwidth," *British Journal of Anaesthesia* (2024).

- 12 D. Martin, C. Johns, L. Sorrell, *et al.*, “Effect of skin tone on the accuracy of the estimation of arterial oxygen saturation by pulse oximetry: A systematic review,” *British Journal of Anaesthesia* (2024).
- 13 Y. Mantri and J. V. Jokerst, “Impact of skin tone on photoacoustic oximetry and tools to minimize bias,” *Biomedical Optics Express* **13**(2), 875–887 (2022).
- 14 M. Moradi, S. Vasudevan, A. Bhusal, *et al.*, “Modeling light-tissue interactions in pulse oximetry: Effect of device design and skin pigmentation,” in *Design and Quality for Biomedical Technologies XVII*, **12833**, 1283302, SPIE (2024). <https://www.spiedigitallibrary.org/conference-proceedings-of-spie/12833/1283302/Modeling-light-tissue-interactions-in-pulse-oximetry--effect-of-10.1117/12.3004189.full>.
- 15 S. Jodging Michael W., Dickson Robert P., Iwashyna Theodore J., *et al.*, “Racial Bias in Pulse Oximetry Measurement,” *New England Journal of Medicine* **383**, 2477–2478 (2020). <https://www.nejm.org/doi/full/10.1056/NEJMc2029240>.
- 16 S. K. N. Swamy, C. He, B. R. Hayes-Gill, *et al.*, “Pulse oximeter bench tests under different simulated skin tones,” *Medical & Biological Engineering & Computing* (2024). <https://doi.org/10.1007/s11517-024-03091-2>.
- 17 S. Chatterjee and P. A. Kyriacou, “Monte Carlo Analysis of Optical Interactions in Reflectance and Transmittance Finger Photoplethysmography,” *Sensors* **19**, 789 (2019). <https://www.mdpi.com/1424-8220/19/4/789>.
- 18 G. Blaney, A. Sassaroli, and S. Fantini, “Method for Measuring Absolute Optical Properties of Turbid Samples in a Standard Cuvette,” *Applied Sciences* **12**, 10903 (2022). [doi.org/10/gsgpzq](https://doi.org/10/gsgpzq).
- 19 G. Blaney, F. Ivich, A. Sassaroli, *et al.*, “Dual-ratio approach for detection of point fluorophores in biological tissue,” *Journal of Biomedical Optics* **28**, 077001 (2023). <https://www.spiedigitallibrary.org/journals/journal-of-biomedical-optics/volume-28/issue-7/077001/Dual-ratio-approach-for-detection-of-point-fluorophores-in-biological/10.1117/1.JBO.28.7.077001.full>.
- 20 G. Blaney, A. Sassaroli, T. Pham, *et al.*, “Phase dual-slopes in frequency-domain near-infrared spectroscopy for enhanced sensitivity to brain tissue: First applications to human subjects,” *Journal of Biophotonics* **13**, e201960018 (2020). <https://doi.org/10.1002/jbio.201960018>.
- 21 A. Sassaroli, G. Blaney, and S. Fantini, “Dual-slope method for enhanced depth sensitivity in diffuse optical spectroscopy,” *Journal of the Optical Society of America A* **36**, 1743–1761 (2019). <https://www.osapublishing.org/abstract.cfm?URI=josaa-36-10-1743>.
- 22 D. M. Hueber, S. Fantini, A. E. Cerussi, *et al.*, “New optical probe designs for absolute (self-calibrating) NIR tissue hemoglobin measurements,” in *Optical Tomography and Spectroscopy of Tissue III*, **3597**, 618–631, SPIE (1999). [doi.org/10/d8vhhm](https://doi.org/10/d8vhhm).
- 23 S. Prahl, “Tabulated Molar Extinction Coefficient for Hemoglobin in Water.” <https://omlc.org/spectra/hemoglobin/summary.html> (1998).

- 24 Q. Fang and D. A. Boas, “Monte Carlo Simulation of Photon Migration in 3D Turbid Media Accelerated by Graphics Processing Units,” *Optics Express* **17**, 20178–20190 (2009). <https://www.osapublishing.org/oe/abstract.cfm?uri=oe-17-22-20178>.
- 25 S. L. Jacques, “Optical properties of biological tissues: A review,” *Physics in Medicine and Biology* **58**, R37–R61 (2013). <https://doi.org/10.1088/0031-9155/58/11/r37>.
- 26 S. L. Jacques, “Erratum: Optical properties of biological tissues: A review (Physics in Medicine and Biology (2013) 58),” *Physics in Medicine and Biology* **58**(14), 5007–5008 (2013).
- 27 E. V. Salomatina, B. Jiang, J. Novak, *et al.*, “Optical properties of normal and cancerous human skin in the visible and near-infrared spectral range,” *Journal of Biomedical Optics* **11**, 064026 (2006). <https://www.spiedigitallibrary.org/journals/journal-of-biomedical-optics/volume-11/issue-6/064026/Optical-properties-of-normal-and-cancerous-human-skin-in-the/10.1117/1.2398928.full>.
- 28 X. Ma, J. Q. Lu, H. Ding, *et al.*, “Bulk optical parameters of porcine skin dermis at eight wavelengths from 325 to 1557 nm,” *Optics Letters* **30**, 412–414 (2005). <https://opg.optica.org/ol/abstract.cfm?uri=ol-30-4-412>.
- 29 R. R. Warner, M. C. Myers, and D. A. Taylor, “Electron Probe Analysis of Human Skin: Determination of the Water Concentration Profile,” *Journal of Investigative Dermatology* **90**, 218–224 (1988). <https://www.sciencedirect.com/science/article/pii/S0022202X88911463>.
- 30 P. Schiebener, J. Straub, J. M. H. Levelt Sengers, *et al.*, “Refractive index of water and steam as function of wavelength, temperature and density,” *Journal of Physical and Chemical Reference Data* **19**, 677–717 (1990). <https://doi.org/10.1063/1.555859>.
- 31 N. Choudhury, R. Samatham, and S. L. Jacques, “Linking visual appearance of skin to the underlying optical properties using multispectral imaging,” in *Photonic Therapeutics and Diagnostics VI*, **7548**, 111–116, SPIE (2010). <https://www.spiedigitallibrary.org/conference-proceedings-of-spie/7548/75480G/Linking-visual-appearance-of-skin-to-the-underlying-optical-properties/10.1117/12.842648.full>.
- 32 V. G. Peters, D. R. Wyman, M. S. Patterson, *et al.*, “Optical properties of normal and diseased human breast tissues in the visible and near infrared,” *Physics in Medicine & Biology* **35**, 1317 (1990). <https://dx.doi.org/10.1088/0031-9155/35/9/010>.
- 33 D. B. Jakubowski, A. E. Cerussi, F. P. Bevilacqua, *et al.*, “Monitoring neoadjuvant chemotherapy in breast cancer using quantitative diffuse optical spectroscopy: A case study,” *Journal of Biomedical Optics* **9**, 230–238 (2004). <https://www.spiedigitallibrary.org/journals/journal-of-biomedical-optics/volume-9/issue-1/0000/Monitoring-neoadjuvant-chemotherapy-in-breast-cancer-using-quantitative/10.1117/1.1629681.full>.
- 34 R. S. Venkata, *Determination of Optical Scattering Properties of Tissues Using Reflectance-Mode Confocal Microscopy*. PhD thesis, Oregon Health & Science University (2012). <https://doi.org/10.6083/M4R78C7S>.

- 35 S. J. Matcher, M. Cope, and D. T. Delpy, “In vivo measurements of the wavelength dependence of tissue-scattering coefficients between 760 and 900 nm measured with time-resolved spectroscopy,” *Applied Optics* **36**, 386–396 (1997). <https://opg.optica.org/ao/abstract.cfm?uri=ao-36-1-386>.
- 36 H. H. Mitchell, T. S. Hamilton, F. R. Steggerda, *et al.*, “THE CHEMICAL COMPOSITION OF THE ADULT HUMAN BODY AND ITS BEARING ON THE BIOCHEMISTRY OF GROWTH,” *Journal of Biological Chemistry* **158**, 625–637 (1945). <https://www.sciencedirect.com/science/article/pii/S0021925819513394>.
- 37 F. Bevilacqua, A. J. Berger, A. E. Cerussi, *et al.*, “Broadband absorption spectroscopy in turbid media by combined frequency-domain and steady-state methods,” *Applied Optics* **39**, 6498–6507 (2000). [doi.org/10/fkk8t3](https://doi.org/10/fkk8t3).
- 38 M. Firbank, M. Hiraoka, M. Essenpreis, *et al.*, “Measurement of the optical properties of the skull in the wavelength range 650-950 nm,” *Physics in Medicine & Biology* **38**, 503 (1993). <https://dx.doi.org/10.1088/0031-9155/38/4/002>.
- 39 G. Alexandrakis, F. R. Rannou, and A. F. Chatziioannou, “Tomographic bioluminescence imaging by use of a combined optical-PET (OPET) system: A computer simulation feasibility study,” *Physics in Medicine & Biology* **50**, 4225 (2005). <https://dx.doi.org/10.1088/0031-9155/50/17/021>.
- 40 B. M. Q. Weaver, G. E. Staddon, and M. R. B. Pearson, “Tissue blood content in anaesthetised sheep and horses,” *Comparative Biochemistry and Physiology Part A: Physiology* **94**, 401–404 (1989). <https://www.sciencedirect.com/science/article/pii/S0300962989901138>.
- 41 J. S. Harrison, P. Rameshwar, V. Chang, *et al.*, “Oxygen saturation in the bone marrow of healthy volunteers,” *Blood* **99**, 394 (2002). <https://doi.org/10.1182/blood.V99.1.394>.
- 42 S. Jacques, “Melanosome Absorption Coefficient.” <https://omlc.org/spectra/melanin/mua.html> (1998).
- 43 S. Jacques, “Extinction Coefficient of Melanin.” <https://omlc.org/spectra/melanin/extcoeff.html> (2018).
- 44 S. Jacques, “Optical Absorption of Melanin.” <https://omlc.org/spectra/melanin/index.html> (2018).
- 45 S. L. Jacques and D. J. McAuliffe, “The Melanosome: Threshold Temperature for Explosive Vaporization and Internal Absorption Coefficient During Pulsed Laser Irradiation,” *Photochemistry and Photobiology* **53**(6), 769–775 (1991). <https://onlinelibrary.wiley.com/doi/abs/10.1111/j.1751-1097.1991.tb09891.x>.
- 46 G. Blaney, A. Sassaroli, and S. Fantini, “Spatial sensitivity to absorption changes for various near-infrared spectroscopy methods: A compendium review,” *Journal of Innovative Optical Health Sciences* , 2430001 (2024). <https://www.worldscientific.com/doi/10.1142/S1793545824300015>.
- 47 G. Blaney, *Enabling Deep Region Specific Optical Measurements in a Diffusive Medium with Near-Infrared Spectroscopy*. PhD thesis, Tufts University, Medford, MA USA (2022). [proquest.com/dissertations-theses/enabling-deep-region-specific-optical/docview/2676526855/se-2](https://proquest.com/dissertations-theses/enabling-deep-region-specific-optical/docview/2676526855/se-2).

- 48 R. Yao, X. Intes, and Q. Fang, “Direct approach to compute Jacobians for diffuse optical tomography using perturbation Monte Carlo-based photon “replay”,” *Biomedical Optics Express* **9**, 4588–4603 (2018). <https://opg.optica.org/boe/abstract.cfm?uri=boe-9-10-4588>.
- 49 R. Aronson, “Radiative transfer implies a modified reciprocity relation,” *JOSA A* **14**, 486–490 (1997). <https://opg.optica.org/josaa/abstract.cfm?uri=josaa-14-2-486>.
- 50 S. Fantini, “Dynamic model for the tissue concentration and oxygen saturation of hemoglobin in relation to blood volume, flow velocity, and oxygen consumption: Implications for functional neuroimaging and coherent hemodynamics spectroscopy (CHS),” *NeuroImage* **85**, 202–221 (2014). <http://dx.doi.org/10.1016/j.neuroimage.2013.03.065>.
- 51 J. M. Kainerstorfer, A. Sassaroli, and S. Fantini, “Optical oximetry of volume-oscillating vascular compartments: Contributions from oscillatory blood flow,” *Journal of Biomedical Optics* **21**, 101408 (2016). <https://www.spiedigitallibrary.org/journals/journal-of-biomedical-optics/volume-21/issue-10/101408/Optical-oximetry-of-volume-oscillating-vascular-compartments--contribut-10.1117/1.JBO.21.10.101408.full>.
- 52 A. Nuttall, “Some windows with very good sidelobe behavior,” *IEEE Transactions on Acoustics, Speech, and Signal Processing* **29**, 84–91 (1981). <https://ieeexplore.ieee.org/document/1163506>.
- 53 E. Monk, “Monk skin tone scale.” <https://skintone.google> (2019).

**Giles Blaney** is a National Institutes of Health (NIH) Institutional Research and Academic Career Development Award (IRACDA) Postdoctoral Scholar in the Diffuse Optical Imaging of Tissue (DOIT) lab at Tufts University. He received his Ph.D. from Tufts University (Medford, MA USA) in 2022 after working in the same lab with Prof. Sergio Fantini as his advisor. Before that Giles received an undergraduate degree in Mechanical Engineering and Physics from Northeastern University (Boston, MA USA). His current research interests include diffuse optics and its possible applications within and outside of medical imaging.

**Jodee Frias** is a second-year Ph.D. student in the DOIT Lab at Tufts University. She is from Avon, MA and received a Bachelor of Science in Biomedical Engineering from Boston University in 2022. During her undergraduate degree, she conducted research on a wearable Short-Wave InfraRed (SWIR) optical probe to monitor hydration in hemodialysis patients. Jodee is currently working on functional Near-InfraRed Spectroscopy (NIRS) measurements, and is extremely interested in non-invasive imaging techniques for clinical applications.

**Fatemeh Tavakoli** is a second-year Ph.D. student in the Diffuse Optical Imaging of Tissue (DOIT) lab under the advisement of Professor Sergio Fantini at Tufts University (Medford, Massachusetts). Her current field of research is Frequency-Domain Near-Infrared Spectroscopy (NIRS) and Diffuse Optics to investigate non-invasive techniques for medical applications, such as hemodynamic monitoring of skeletal muscles and brain function. Before that, she received an M.Sc. degree in Electrical Engineering from Islamic Azad University, Science and Research Branch, in 2020 (Tehran,

Iran). During her master's degree, she found Fractal geometry to be a unique way of looking at the world, and she successfully designed a perfect absorber based on self-similar nanoparticles, allowing for tuning optical properties for near-infrared applications.

**Angelo Sassaroli** received a Ph.D. in Physics in 2002 from the University of Electro-Communications (Tokyo, Japan). From July 2002 to August 2007, he was a Research Associate in the research group of Prof. Sergio Fantini at Tufts University. In September 2007 he was appointed by Tufts University as a Research Assistant Professor. His field of research is near-infrared spectroscopy and diffuse optical tomography.

**Sergio Fantini** is a Professor of Biomedical Engineering and Principal Investigator of the DOIT at Tufts University. His research activities on applying diffuse optics to biological tissues resulted in about 120 peer-reviewed scientific publications and 12 patents. He co-authored with Prof. Irving Bigio (Boston University, Boston, MA USA) a textbook on "Quantitative Biomedical Optics" published by Cambridge University Press in 2016. He is a Fellow of SPIE, Optica, and the American Institute for Medical and Biological Engineering (AIMBE).